Triangulation of Pore Structural Characterisation of Disordered Mesoporous Silica Using Novel Hybrid Methods Involving Dual-Probe Porosimetries

Suleiman Mousa[a], Kyro Baron[a], Robin S. Fletcher[b], Sean P. Rigby[a,c,*]

[a]Department of Chemical and Environmental Engineering, Faculty of Engineering, University of Nottingham, University Park, Nottingham, NG7 2RD, U.K.

[b]Johnson Matthey, P.O. Box 1, Belasis Avenue, Billingham, Cleveland, TS23 1LB, U.K.

[c]Geo-energy Research Centre, University of Nottingham, University Park, Nottingham, NG7 2RD, U.K.

*Corresponding author: Email: sean.rigby@nottingham.ac.uk

ABSTRACT

The key issue, in applying indirect pore structure characterisation methods to disordered materials, is that usually some physical assumptions are necessary to probe pore size, such as concerning the mode of the phase transition used, which determines meniscus geometry or kernel type. This issue often undermines the relative advantages of indirect methods, over direct methods like imaging, from both the wider range of pores sizes that can be probed in a single experiment and the much better statistical representativeness of the data, which are essential for highly heterogeneous disordered materials. Further, parameter calibrations provided using supposedly the same model ordered porous materials are often conflictual. However, this work introduces dual-liquid thermoporometry, and also dual-probe, serial water sorption and mercury intrusion, to complement multi-adsorbate, serial gas sorption, to overcome this issue by triangulating the data for three key probe molecules used in three different porosimetries, namely liquid intrusion, gas sorption, and thermoporometry. It has been found that augmenting one porosimetry, using just one probe molecule, to a dual-probe experiment removes the aforementioned, key drawback of indirect methods. The alternative, complementary dual-probe porosimetries can also cross-validate this approach for each other. This allows indirect methods to stand alone, without the need for direct imaging methods to inform or validate prior assumptions. Further, the dual-probe experiments allow additional information on pore structure to be obtained beyond that provided by single-probe experiments. For example, dual-liquid thermoporometry also allows the probing for the presence and nature of the advanced melting effect, and serial water adsorption and mercury porosimetry delivers information on network filling mechanisms during adsorption in disordered media.

1 INTRODUCTION

A single method can never adequately shed light on a given natural phenomenon, and this is true for both direct and indirect pore structural characterisation methods. Indirect pore structural characterization methods, such as mercury porosimetry, gas sorption, and thermoporometry, maintain many advantages over more direct methods, such as imaging [1]. Indirect methods can characterise a much broader range of pore sizes, from millimetres down to molecular scales, all in the same experiment, and quickly obtain data on nanoporosity for a more statistically-representative sample volume than the fields-of-view possible in all imaging modalities [1]. However, being indirect, the accuracy of void space descriptors obtained via these methods relies upon the validity of key parameters in the relationship between pore size and the relevant control variable, such as temperature in thermoporometry, and choices in the data analysis that reflect the basic geometry of the void space, such as pore shape. Further, the physical processes used for characterisation, such as capillary condensation in gas sorption, are more complex in disordered, amorphous materials than they are in templated, model materials, such as high-quality MCM-41 or SBA-15, with much simpler void space geometries [1]. In disordered networks, pore-to-pore co-operative processes, such as advanced condensation or advanced melting, can occur, and complicate data analysis. However, these additional effects can also be harnessed to deliver additional information on complex void spaces [1]. Hence, there is a need for experimental and data analysis procedures to address these issues. This paper will present a triangulation procedure, involving three different probes, nitrogen, water and mercury, to validate pore space characterisations from different indirect methods.

Previous work has shown that the key parameters in the master equations relating control variables to pore sizes, such as the Gibbs-Thomson constant (K) in thermoporometry, obtained from purported calibrations using model templated porous solids give rise to different values, depending upon the particular type of model, controlled pore size material used, and the value of the thickness of the non-freezing surface layer taken. For example, Gun'ko et al. [2] suggested K for melting of water in silica pores was 67 K nm, but does not report how this value was obtained. In contrast, Findenegg et al. [3] suggested K was 52±2 K nm. From a survey of the relevant literature, Rottreau et al. [4] found that the range of K values previously obtained for water lies between 49 and 58 K nm. A related issue is that indirect methods require an assumption of pore geometry, which implicitly makes assumptions about the meniscus geometry for the vapour/liquid, or liquid/solid, boundaries, where one phase expands at the expense of the other, during characterisation experiments. However, in the aforementioned case, the discrepancy (of ~30 %) in Gibbs-Thomson constant cannot be simply explained by

suggesting melting occurs radially via a hemispherical meniscus in one case, but axially via a cylindrical sleeve meniscus in another, since then that difference in *K* would be expected to be a factor of 2 [5-7]. This discrepancy suggests that the calibration based upon model templated materials is not always generalisable, and, thence, must be performed each time for the exact material under test, including for difficult disordered materials. While an electron micrograph may reveal the particular pore geometry, even for micropores, for a small region of sample void space, this may not be representative of the whole sample volume, or of different pore sizes. The mode of phase transition, relating to meniscus geometry for simple pore shapes, must be determined via a more generally applicable way.

Additional effects, other than single pore phenomena, occur during the phase transitions employed for indirect structural characterisation of disordered pore networks. While this adds to the complexity of data interpretation, these additional effects can be used to obtain extra information about pore spaces. From a study using scanning curves, Everett [8] showed that gas desorption from disordered porous solids can involve a pore-to-pore co-operative effect known as ‘pore-blocking’ (or pore-shielding or pore shadowing), which has since widely been employed, together with percolation theory, to determine pore network connectivity [9-11]. While Gregg and Sing [12] explained why adsorption is not similarly affected by pore-blocking, it is affected by two other pore-to-pore co-operative effects, namely advanced condensation and (network) delayed condensation [1,13].

The effect, now variously known as advanced condensation, advanced adsorption, or the cascade effect, was first published upon by de Boer [14]. The simplest operation of these effects occurs for a through ink-bottle pore geometry consisting of two relatively narrow cylindrical pore necks either side of, and co-axial with, a larger cylindrical pore body. In the classical interpretation of gas adsorption, capillary condensation in such a system is initiated in the pore necks via a cylindrical sleeve meniscus, which then completes a hemispherical meniscus at both ends of the pore body. If the diameter of the pore body is less than twice that of the pore necks, then the gas pressure needed to fill the necks also exceeds that to fill the pore body with condensate via axial expansion of the hemispherical menisci. Hence, necks and body will fill simultaneously at the same pressure. If the pore body diameter exceeds twice that of the neck, while the pore body does not fill at the same pressure as the necks, the pressure needed to fill it is then still lower than for if the pore body were part of a parallel pore bundle (a ‘wine rack-type’ structure). This bundle is the standard pore space model, for pore size distribution (PSD) derivation by gas sorption, used by both classical and DFT-based approaches [15]. Hence, PSDs

for disordered materials obtained by standard methods can be inaccurately skewed towards smaller pores [1]. It has also been found [16] that the width of single-pore hysteresis in gas sorption for cylindrical pores does not match the predictions of either the Cohan [17] equations or of non-local density functional theory (NLDFT) [18]. This is an empirical indication that additional effects are at work than encompassed by these theories. The detection of the presence and extent of advanced adsorption effects is essential to obtain accurate PSDs, and this has been done in the past using NMR methods [19].

An analogous effect to advanced adsorption, known as advanced melting, has been proposed to occur in thermo-/cryo-porometry [7]. In a through ink-bottle pore full of probe fluid, the melting of solidified probe fluid within the pore necks occurs at the temperature required for the radial expansion of the cylindrical sleeve-shaped non-freezing layer, left at the pore-matrix interface, toward the centreline of the necks [5]. On completion, this then creates full hemispherical menisci between liquid and solid at both ends of the pore body. Melting can then occur at the same temperature in the pore body by axial advancement of these solid-liquid menisci if the pore body diameter is less than twice the pore neck diameter. The advanced melting effect has been observed in a range of disordered materials, including mesoporous catalysts [7] and cements [20].

While, as mentioned above, the various pore-to-pore co-operative effects in disordered networks potentially complicate data analysis and interpretation, their idiosyncratic features mean that their impact can be potentially deconvolved with the right datasets [1, 13]. For example, while advanced adsorption and melting only conceals the presence of pore bodies for body sizes up to twice that of the neck (according to classical theory like the Kelvin equation), the pore-blocking effect can conceal pore bodies of any size behind the neck. Further, while advanced adsorption or advanced melting can occur in any direction, including inwards, the pore-blocking effect only acts in the direction of the percolation path to the exterior.

The aforementioned issues with gas sorption, mercury porosimetry and thermoporometry for amorphous materials, namely calibration, pore geometry, and pore-to-pore co-operative effects, only present problems with the conventional experiments as conducted with these techniques [1, 13]. These conventional experiments are only run in parallel and typically only produce boundary adsorption/desorption isotherms, or boundary melting/freezing curves, or boundary intrusion/extrusion curves, for samples empty of anything but a single probe fluid. However, it is possible to combine these different techniques into hybridised methods consisting of serial experiments with different probes run on the same sample with little or no intermediate sample

preparative treatment [1, 13]. In this manner, the void space under test is modified in a controlled way, and this changes the results of applying a given technique with a particular probe fluid, and this change can elucidate the mechanisms involved in both the modification and probe processes. In this work we have greatly expanded the repertoire of hybrid methods run on the same sample and material from previous studies [1, 13]. We have conducted novel thermoporometry experiments with multiple, immiscible probe liquids within the same sample. In addition, we have conducted the serial adsorption of water before mercury porosimetry, where the adsorbed water was retained during porosimetry, and then nitrogen adsorption afterwards on the same sample by freezing the pre-adsorbed water and entrapped mercury in-place. These have been augmented with serial adsorption of first nitrogen, second water, then nitrogen, and integrated nitrogen sorption and mercury porosimetry [21]. The hybrid experiments force the confrontation of the data from different techniques for the same sample, and enable parameter calibration and appropriate phase transition mode selection, even for amorphous solids.

Figure 1. Schematic diagram illustrating the triangulation strategy adopted in this work.

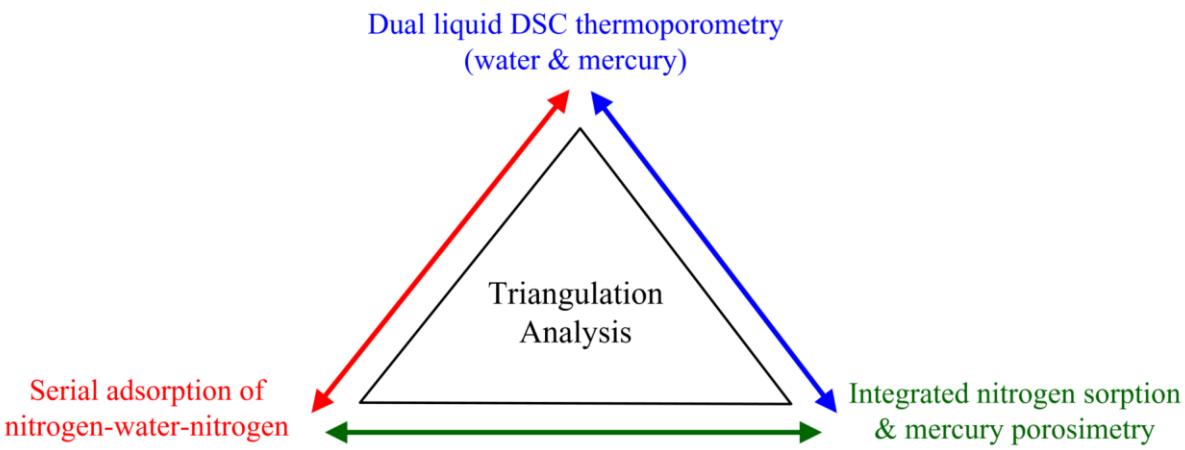

Thermoporometry (or cryoporometry) with two different liquids has been performed previously but with the aim of studying the progress of liquid-liquid displacement or separation of miscible binary mixture components [22-24]. These studies focussed simply on the apparent relative pore sizes occupied by each of the two liquids involved, and, thus, did not consider the details of the phase transitions in the two liquids. In this work the mode of the phase transition in each liquid, and any interactions, will be considered in much more detail.

The new methods described here are trialled in a case study of a disordered, mesoporous, sol-gel silica material. Single-probe thermoporometry and gas sorption have been extensively used, in a solely parallel fashion, for pore structure characterisation of silica gel materials [2,3,25,26]. However, here, dual-liquid (water plus mercury) thermoporometry, serial water adsorption-and-mercury-porosimetry, serial nitrogen-and-water sorption, and integrated nitrogen sorption-and-mercury-porosimetry experiments were all conducted on the sol-gel silica material. The data from all these experiments were then analysed synergistically. This is shown schematically in **Figure 1**. **Figure 1** shows the three probes used to triangulate findings, and the various hybrid experiments which use each probe.

Given water is used as one of the three key probes in this work, it is important to properly understand its mode of adsorption in the type of material under study. Water sorption has the advantage that it can be used without extensive pre-drying for already partially water wet samples like cement pastes [27]. While water vapour sorption is widely used for pore structure characterisation of disordered materials [27], the particular mode of water adsorption is sometimes suggested [12] to be as localised ganglia, rather than as a more pervasive multi-layer, on silicas. Hence, the structure of the adsorbed water film will be studied in detail using serial nitrogen adsorption.

2 THEORY

2.1 Gas sorption

2.1.1 Adsorbed films on fractally rough surfaces

The surface of amorphous silicas is known to be fractally rough [28]. The surface area A of an adsorbed film of general thickness z is related to the volume V of that film by [29]:

$$A(z) = \frac{dV}{dz}. \quad (1)$$

In the special case where the surface of the solid is fractal, with surface fractal dimension D, then, $V(z)$ is proportional to z^{3-D} and therefore $A(z)$ is proportional to z^{2-D} by eq 1. Hence, by eliminating z from these relations for V and A, then:

$$A \propto V^{(2-D)/(3-D)}. \quad (2)$$

Hence, the film area on a fractal surface ($D > 2$) will decrease with increasing film volume (and increasing z) as the film smooths out the roughness of the solid surface. Further, since the film itself and the residual pore volume, exterior to the film, share a mutual boundary, then the surface area of the residual pore space will correspondingly decrease with decreasing residual pore volume. Hence, the residual pore volume might be expected to follow a reciprocal relationship to eq. (2).

2.1.2 Capillary condensation

Capillary condensation of the probe gas in isolated cylindrical meso- and macro-pores is predicted by the Kelvin equation [12, 15]:

$$ln\left(\frac{P}{P_0}\right) = -\frac{k\gamma V_M cos\theta}{RT(r_p - t)} = \frac{-kF}{(r_p - t)} \quad , \quad (3)$$

where P/P_0 is the relative pressure at which capillary condensation occurs in a cylindrical pore of radius r_p, t is the multilayer film thickness, k is a geometrical parameter dependant on the pore and meniscus type (for adsorption within a cylindrical pore open at both ends $k = 1$; and for adsorption within a pore with one dead end, or for desorption from a hemi-spherical meniscus, $k = 2$), γ is the surface tension, V_m is the molar volume of the condensed adsorbed phase, θ is the contact angle with which the condensate meets the wall, and T is the absolute temperature. F is a combined adsorbate property factor. The contact angle is generally assumed to be zero for wetting adsorbates. The two forms of the Kelvin equation, with different types of meniscus geometry on adsorption, are known as the Cohan [17] equations. The term $\gamma V_M/RT$ for nitrogen (component 1) at 77 K is 0.48 nm, while that for water (component 2) at 293 K is 0.54

nm. Hence, for adsorption in the same pore geometry the relative pressures for two different adsorbates are related by:

$$ln\left(\frac{P}{P_0}\right)_1 = \frac{F_1}{F_2} ln\left(\frac{P}{P_0}\right)_2, \quad (4)$$

For calculating the nitrogen pore size distributions (PSDs) used here, the Barrett-Joyner-Halenda [30] algorithm and the Harkins-Jura [31] *t*-layer equation were used.

2.2 Thermoporometry

Petrov and Furó [5] attributed freezing-melting hysteresis in cryoporometry to a free energy barrier between metastable and stable states of pore filling material. In a phenomenological description, these workers showed that freezing point depression is given by:

$$\Delta T_f \cong -\frac{\upsilon \gamma_{sl} T^0}{\Delta H} \frac{S}{V}, \quad (5)$$

while the melting point depression is given by:

$$\Delta T_m \cong -\frac{\upsilon \gamma_{sl} T^0}{\Delta H} \frac{\partial S}{\partial V}, \quad (6)$$

where υ is the molar volume, γ_{sl} is the surface free energy, T^0 is the bulk melting point, ΔH is the latent heat of melting, S is the surface area of the pore and V is the volume of the pore. Using Steiner's formula for equidistant surfaces, Petrov and Furó [5] showed that eq. (6) can be rewritten as:

$$\Delta T_m \cong -\frac{\upsilon \gamma_{sl} T^0}{\Delta H} 2\kappa = \Delta T_f \frac{2\kappa V}{S} = \frac{K}{(d-2t)} \quad (7)$$

where κ is the integral mean curvature of the pore surface. For a cylindrical pore of diameter d, then $2\kappa V/S=1/2$, and, hence, the numerical difference in ΔT_m and ΔT_f can be used to determine whether a pore has an open cylindrical geometry. Implicit in eq. (7), is the conception that, upon freezing, liquid solidifies in an axial direction initiated from the end where the liquid is in contact with bulk solid, while melting commences at the liquid film at the pore surface and propagates radially from the surface toward the pore bulk. However, for a dead-end cylindrical pore, melting can occur axially, since it would then be initiated from the hemispherical meniscus at the closed end of the pore. Similarly melting can be initiated from a hemispherical meniscus located at the interface between frozen and molten phases within co-axial, adjoining cylindrical pores of differing diameters [1].

The non-freezing *t*-layer thickness was assumed to be a molecular monolayer. Given the modal size (~10 nm, so ~33 times the size of 1 water molecule) of the pores of the material studied here, the variation in the *t*-layer thickness (with temperature and/or pore size) in thermoporometry observed in the literature [4,25] is much smaller than the impact of an axial versus radial mode for the phase transition. Similarly, the impact of the variation in supercooled water and ice densities, interfacial tension, and latent heats, with temperature are small [25], compared to the phase transition mode effect.

2.3 Small angle X-ray scattering (SAXS)

The intensity of X-ray radiation scattered by a fractal surface is known to be proportional to a negative power of the q vector, such that [1,28]:

$$I(q) \propto q^{-\eta}, \qquad (8)$$

where $q = 4\pi\lambda^{-1} \sin(\varphi/2)$, λ is the wavelength of the radiation, and φ is the scattering angle. Normally this behaviour is only observed if q satisfies the inequality $q\xi >> 1$, where ξ is the characteristic length-scale for the structure creating the scattering. From the value of η, the fractal nature of the system under investigation can be determined [1,28]. If the exponent is in the range $1 < \eta < 3$, then it describes the mass fractal of dimension $(D_m)_{SAXS} = \eta$, but if in the range $3 < \eta < 4$ then it describes surface fractals of dimension $(D_S)_{SAXS} = 6 - \eta$. For $\eta = 4$, Equation (8) leads to Porod's law, where $(D_S)_{SAXS} = 2$ and the surface is flat.

3 MATERIALS AND METHODS

3.1 Silica materials

The sample studied in this work is a commercially-available, spherical, silica catalyst support, denoted G1, made by the sol-gel method. The sol-gel silica spheres have particle sizes in the range 2-7 mm, with the most common size being ~3-4 mm.

3.2 Serial water pre-adsorption, mercury porosimetry, and nitrogen adsorption

Figure 2. A schematic representation of the serial water pre-adsorption, mercury porosimetry and nitrogen adsorption experiment.

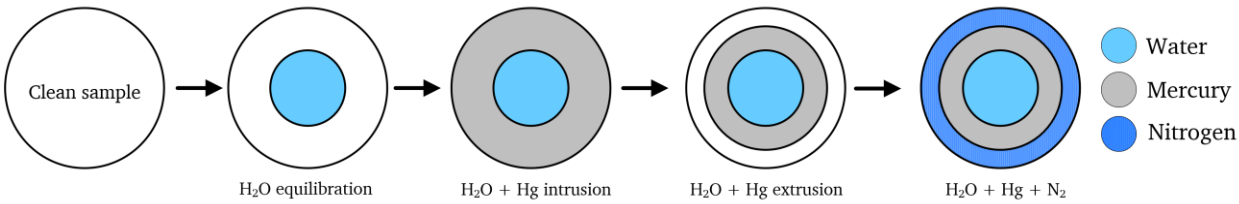

The samples were heated to 90°C at 10°C/min and held for 60 minutes once the pressure had reduced to 100 mmHg. The temperature was then increased to 350°C at 10°C/min and the samples held under vacuum for 16 hrs. The samples were then cooled under vacuum and backfilled with dry nitrogen. Aliquots of the sample were then exposed to a water relative pressure of 0.85 using a saturated solution of potassium chloride. The samples were placed on a watch glass in a single layer next to a beaker of the saturated solution and enclosed within a small, sealed container for eight days. The samples were weighed before and after exposure.

Mercury intrusion/extrusion curves were measured on a Micromeritics AutoPore 9600 porosimeter between 0.0014 and 414 MPa for the intrusion followed by extrusion to 0.1034 MPa. Studies showed that, for samples containing pre-adsorbed water, an equilibration interval of 60 seconds was optimum. A prerequisite for a conventional mercury porosimetry experiment is for the sample to be dried to completely remove any adventitiously adsorbed species. The porosimeter evacuates the sample to less than 25 μmHg to facilitate filling of the sample cell with mercury prior to intrusion. For the samples containing pre-adsorbed water it was found that the evacuation stage would slow considerably and steady out at about 800 μmHg. At this point the pre-adsorbed water is being slowly removed which is defeating the object of the study. For

all runs using samples containing pre-adsorbed water the evacuation step was halted at 1000 μmHg. This pressure ensured water was not removed from the sample porosity and still allowed the sample cell to fill correctly with mercury. It is noted that water is considerably more wetting of the silica surfaces than mercury. Indeed, immersion of a silica-gel sphere containing entrapped mercury into a water bath leads to water displacing the mercury completely from the pores and out into the water bath.

Nitrogen adsorption-desorption isotherms were measured at liquid nitrogen temperature on a Micromeritics ASAP2420 physisorption analyser over the relative pressure range of 0.005 to 0.995 for adsorption and back down to 0.005 on the desorption. To measure the isotherms for samples containing pre-adsorbed water and post mercury porosimetry, the liquid nitrogen dewars were raised around the samples for 30 minutes to freeze the liquids inside the pores before opening the sample port to vacuum. Once the samples were fully evacuated the analysis was initiated. Backfilling of the sample at the start of the analysis was omitted, as was the lowering of the dewar post free space analysis, to prevent the samples warming and thawing the frozen water and/or mercury. This is a departure from normal operation. An equilibration interval of 60 seconds was used rather than the typical value of 10 seconds for a fully outgassed mesoporous material. **Figure 2** shows the schematic representation of the serial water pre-adsorption, mercury porosimetry and nitrogen adsorption experiment.

3.3 Serial adsorption of nitrogen-water-nitrogen

Figure 3. A schematic representation of the integrated nitrogen-water-nitrogen technique. ISO = isotherm,and ROA = rate of adsorption (not considered here)

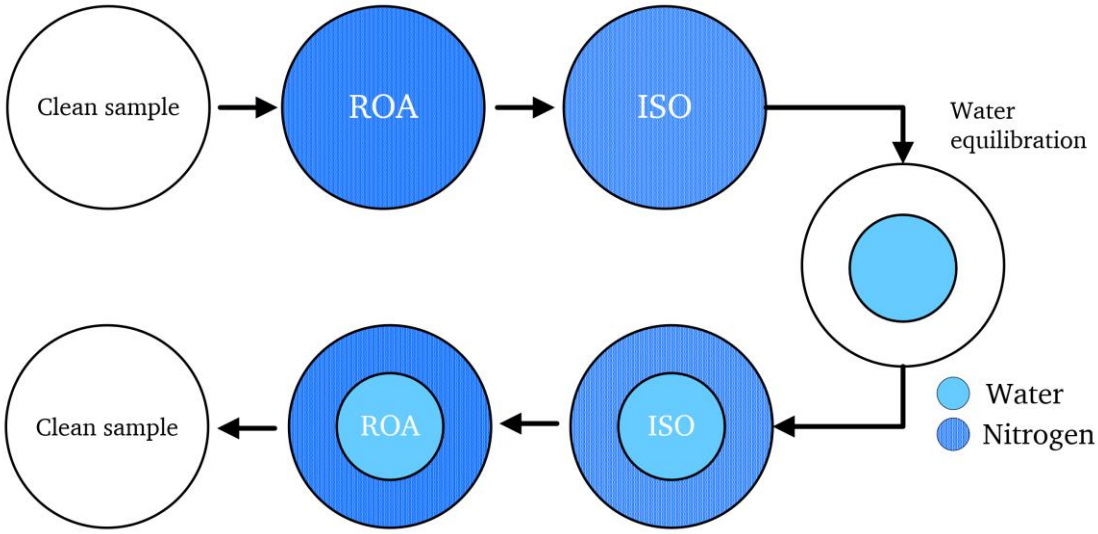

The integrated water and nitrogen technique consists of a series of experiments conducted on the same sample. **Figure 3** shows the schematic representation of the nitrogen-water-nitrogen procedure used during the experiments. The nitrogen sorption isotherms were measured at liquid nitrogen temperature (77 K) using a Micromeritics 3Flex physisorption analyser. Approximately 0.1 g of the sample was weighed and placed into a pre-weighed standard physisorption sample tube with a sealing frit placed at the top to prevent the sample from being evacuated into the 3Flex manifold. The tube (with sample) was then loaded into the degassing station and initially degassed at room temperature until a vacuum of 0.002 mmHg was reached. The sample temperature was then raised to 110°C by using a heating mantle, and the sample was left under vacuum for 24 hours. The thermal pre-treatment drives off any physisorbed water on the sample but does not change the sample morphology. After the 24 hours had passed, the heating mantle was removed, and the sample was allowed to cool down to room temperature. This sample pre-treatment procedure was compared with that mentioned in Section 3.2 and no difference was observed in resultant nitrogen BET surface area. The sample tube and its contents were then re-weighed to obtain the dry weight of the sample. Isothermal jackets were then placed around the sample tubes before reattaching to the analysis port to begin the automated gas sorption analysis. The isothermal jacket ensures a constant thermal profile of 77 K along the length of the sample tube during the analysis stage. Nitrogen purity was 99.995%. Gas sorption was measured over the relative pressure (P/Po) range of 0.01 to 0.995 for

adsorption isotherm and 0.995 to 0.10 for desorption isotherm. The saturation pressure (Po) was measured for each data point on the isotherm.

Once the first nitrogen gas sorption experiment was finished, the samples were allowed to reach room temperature (~295.15 K) and then suspended over a sodium hydroxide solution with a varying concentration (to achieve the desired vapour pressure) for up to ~7 days.

Once the water equilibration experiment was finished, the sample was immediately weighed and returned to the 3Flex sample tube, where the conventional adsorption experiments were repeated. The sample was first cooled to 77 K by manually raising the Dewar flask, allowing the sample to freeze for approximately 30 min. This part was important in the post water entrapment steps since it freezes the water in-place to ensure that it all remains immobilised within the pellets.

3.4 Dual liquid, differential scanning calorimetry (DSC) thermoporometry using water and mercury

Figure 4. A schematic representation showing the dual-liquid DSC thermoporometry procedure.

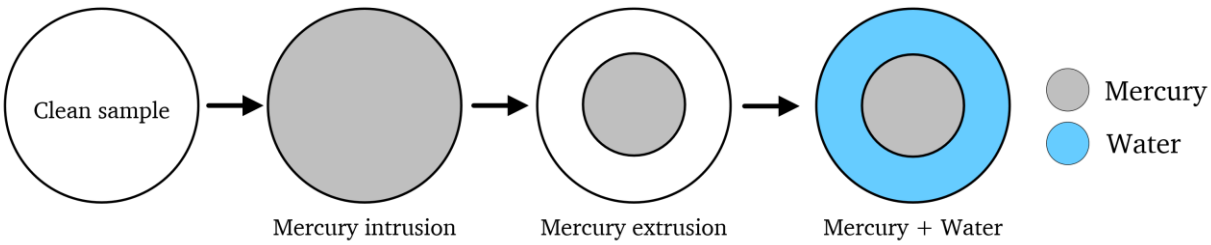

For the dual-liquid experiments, the samples were first entrapped with mercury using mercury porosimetry and then immersed into a deionised water bath. Mercury intrusion and retraction curves were measured using a Micromeritics Autopore IV 9500, which can generate a maximum pressure of 414 MPa (= 60000 psia). The mercury intrusion data was generated for up to 60000 psia, followed by retraction down to atmospheric pressure. A clean sample was first transferred into a penetrometer, and the weight of the penetrometer and sample was recorded. The penetrometer (with sample) is then placed in the low-pressure port of the instrument. During the low-pressure analysis, the sample is firstly evacuated up to 50 mmHg to drive off

any water vapour or atmospheric gases in the pore network. The sample bowl is then filled with mercury while the entire system is still under low pressure. Data collection begins at a pressure of 0.5 psia, which is enough pressure to cause mercury to penetrate sample pores bigger than 360 μm in diameter. After the low-pressure analysis was completed, the assembly weight (penetrometer + sample + mercury) was recorded, the penetrometer was transferred to the high-pressure port, and the chamber was closed tightly. The penetrometer is placed vertically in the high-pressure port, and it is surrounded by oil, which is the hydraulic fluid the instrument uses to generate high pressures. As the hydraulic fluid pressure rises, it is transmitted to the mercury in the penetrometer via its open capillary stem. An equilibration time of 15s was used for each data point.

Once the mercury porosimetry experiment was finished, the samples with mercury were immediately immersed into a deionised water bath for 5, 30 and 60 or 300 s. The samples were then placed inside a high-volume steel pan to run the DSC thermoporometry experiments. The DSC melting-freeze experiments were performed in TRIOS DSC2500 equipped with a cooling and data process system. A small drop of the probe liquids was also placed in the pans in every experiment. This droplet of liquid acts as a reference peak for the melting bulk liquid outside the sample pores. The pans with the samples were then loaded into the machine at room temperature (~ 21 °C) and frozen to the required temperature of -80 °C, immediately. To achieve temperature homogeneity and account for the differences between the actual temperature inside the pores and the sensor temperature, the samples were kept at this temperature for 30 min. After the samples reached thermal equilibration, the data points for the melting curves were measured over the range from -80 °C to 10 °C at different ramping rates of 0.1 °C/min, 0.25 °C/min and 0.5 °C/min. However, a further increase in the ramping rate caused a shift in the melting peak temperature towards the bulk peak, and therefore, only the first three ramping rates listed were used. **Figure 4** shows a schematic representation of the novel dual liquid DSC experiment procedure. Multiple freeze-thaw cycles were used to check for any structural modification arising from mechanical damage during freezing, but none was observed.

3.5 Integrated nitrogen sorption and mercury porosimetry

The method consists of serial gas sorption and mercury porosimetry experiments conducted on the same sample. The method used here has been described previously in Rigby et al. [21].

4 RESULTS

4.1 Adsorbent characteristics

Figure 5 shows atomic force microscopy (AFM) images of a typical sample of G1. From Figure 5(a), it can be seen that the larger-scale structure consists of a botryoidal aggregate of brighter white globular particles, surrounded by narrow darker regions. From the higher resolution image in Figure 5(b), it can be seen that there are brighter regions, corresponding to constituent particles, with darker surrounding regions corresponding to necks between the particles, that are highly fused. Hence, it can be seen that the basic structure of G1 consists of a partly sintered packing of the original sol spherical particles of the sol-gel synthesised material.

Figure 5. Larger **(a)** and smaller **(b)** length-scale AFM images of typical samples of G1 sol-gel silica showing the pore-scale morphology of the materials and the typical constituent particle size.

(a)

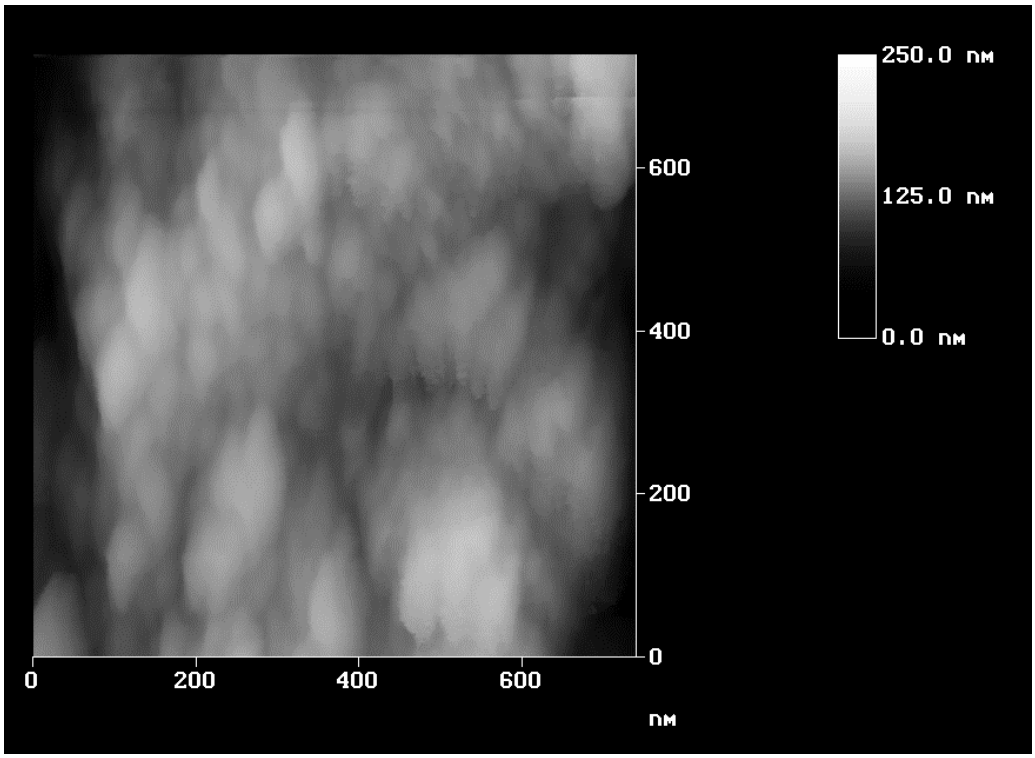

(b)

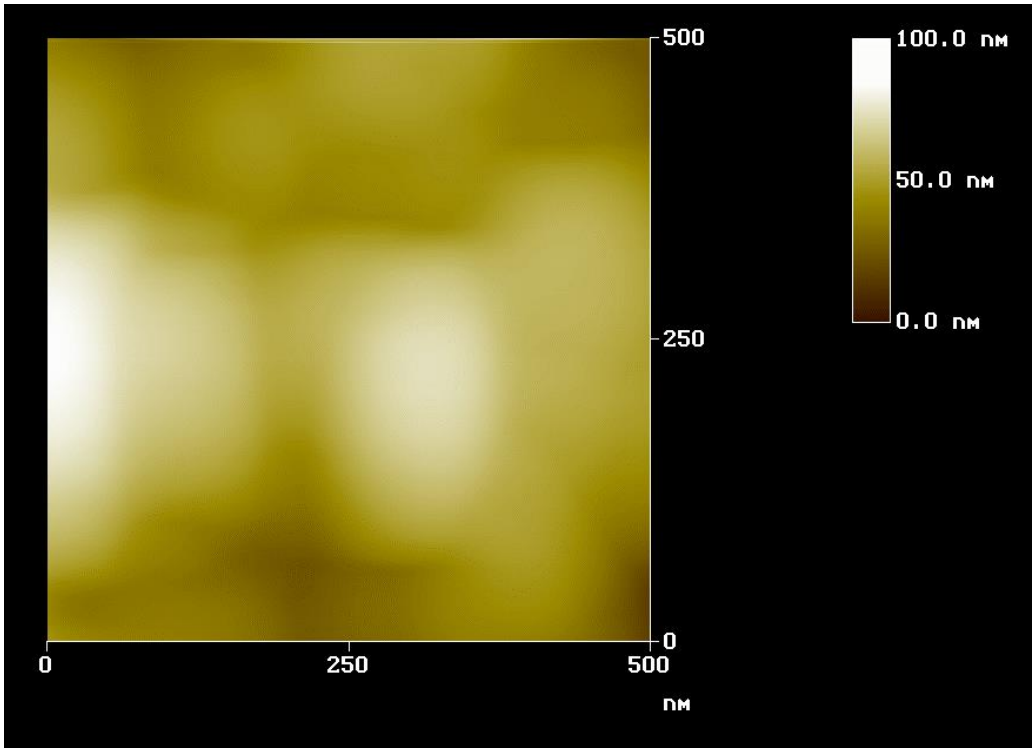

Table 1 shows the parameters obtained previously [28] from fits of the (fractal) Porod law (eq. 8) to SAXS data for samples of pellet G1. It suggests that the average surface fractal dimension below ~1 nm is equal to 2.1, while above ~1 nm is 2.4.

Table 1. Parameters obtained previously [28] from fits of the (fractal) Porod law to SAXS data for samples of pellet G1

Sample fractal dimension	***q*/nm^{-1}**	**Length-scale cut-offs/nm**
1.977±0.004	0.626-3.23	0.31-1.60
2.246±0.004	1.0-3.54	0.28-1.0
2.34±0.04	0.566-0.997	1.0-1.768
2.51±0.05	0.503-0.998	1.0-1.988

4.2 Serial nitrogen-water-nitrogen adsorption

Figure 6 shows the nitrogen sorption isotherms obtained both before and after adsorbing water to relative pressures of 0.497, 0.646, 0.794, 0.871 and 0.914, and then freezing in-place. The nitrogen sorption isotherms obtained after water adsorption have been adjusted upwards in amount adsorbed, and it was found that they could be overlaid completely on top of the isotherms obtained for dry samples for the highest amounts adsorbed.

Figure 6. Nitrogen sorption isotherms obtained both before (solid line) and after (×) adsorbing water to relative pressures of (a) 0.497, (b) 0.646, (c) 0.794, (d) 0.871 and (e) 0.914, and then freezing in-place. The nitrogen sorption isotherms obtained after water adsorption have been adjusted upwards in amount adsorbed such that they overlay completely the top of the isotherms obtained for dry samples for the highest amounts adsorbed. The locations of the deviations of the two sets of isotherms are indicated.

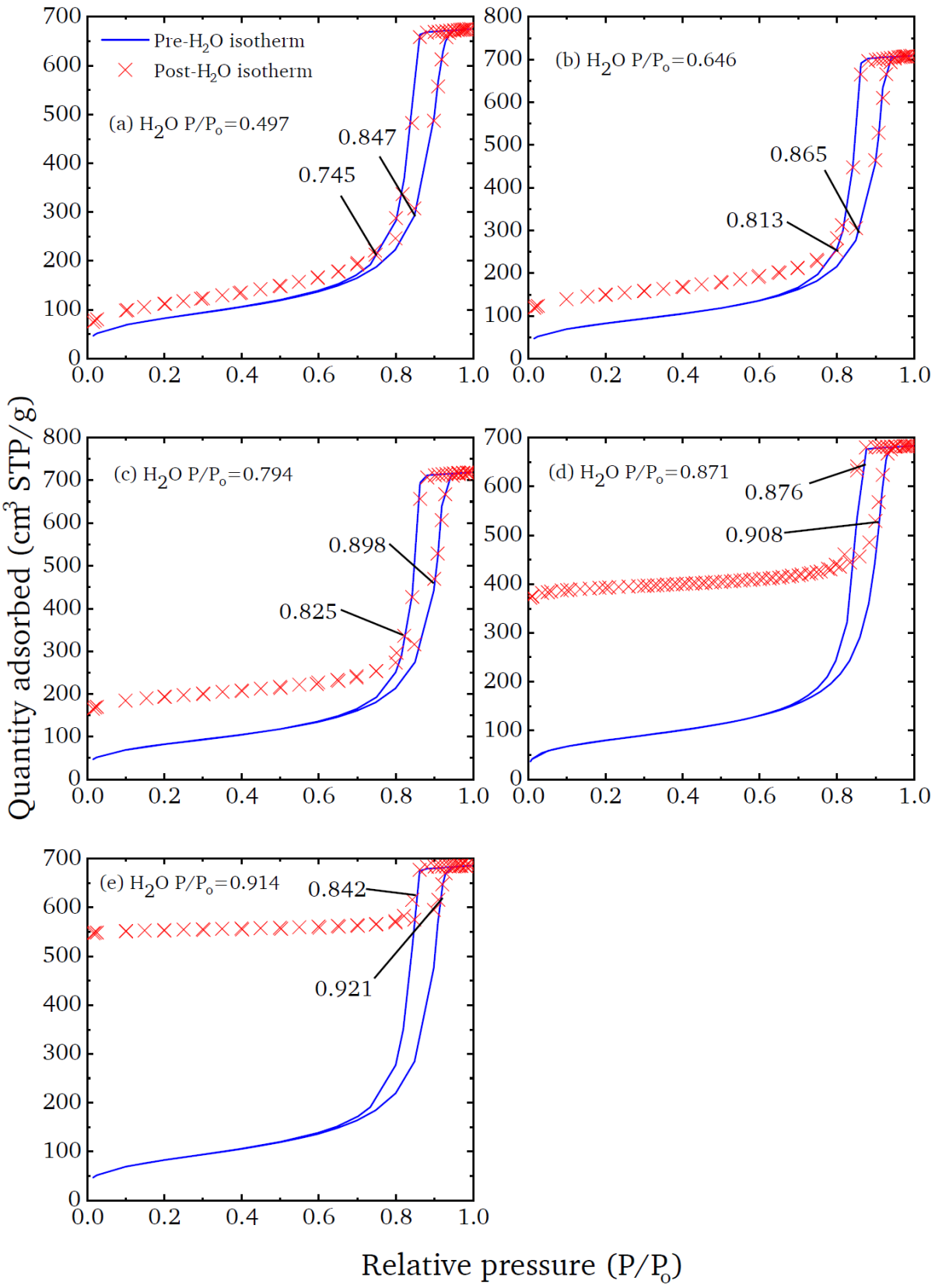
Pre-H2O isotherm
Post-H2O isotherm
(a) H2O P/Po=0.497
0.847
0.745
(b) H2O P/Po=0.646
0.865
0.813
(c) H2O P/Po=0.794
0.898
0.825
(d) H2O P/Po=0.871
0.876
0.908
(e) H2O P/Po=0.914
0.842
0.921
Quantity adsorbed (cm3 STP/g)
Relative pressure (P/Po)

1

2

Figure 7 shows water sorption isotherms obtained for G1. Also shown is a fit of the fractal BET isotherm [1,28] for relative pressures less than 0.5, where the hysteresis starts indicating the possible onset of capillary condensation. In order to put the adsorption behaviour of nitrogen and water on G1 in a broader context, adsorption isotherms were also obtained for argon, propane, n-butane, n-hexane, and cyclohexane, and are given in **Appendix A1**. The isotherms for fresh G1 in **Figure 6**, together with those in **Appendix A1**, were all fitted to both the fractal BET and fractal FHH isotherms [1, 28]. Examples (for fractal BET) of the results of these fits to the isotherms are given in **Appendix A1**, and the fitted parameters obtained for both models are given in **Table 2**. From **Table 2**, it is noted that the fractal dimensions from the fractal BET fits are similar to those for short length-scales from SAXS for all adsorbates except nitrogen. However, it is noted that the fractal dimensions for cyclohexane and n-hexane are noticeably lower than for other adsorbates.

Figure 7. Water adsorption (◆) and desorption (■) isotherms obtained at 283 K. Also shown (solid line) is a fit of the fractal BET isotherm for relative pressures <0.5.

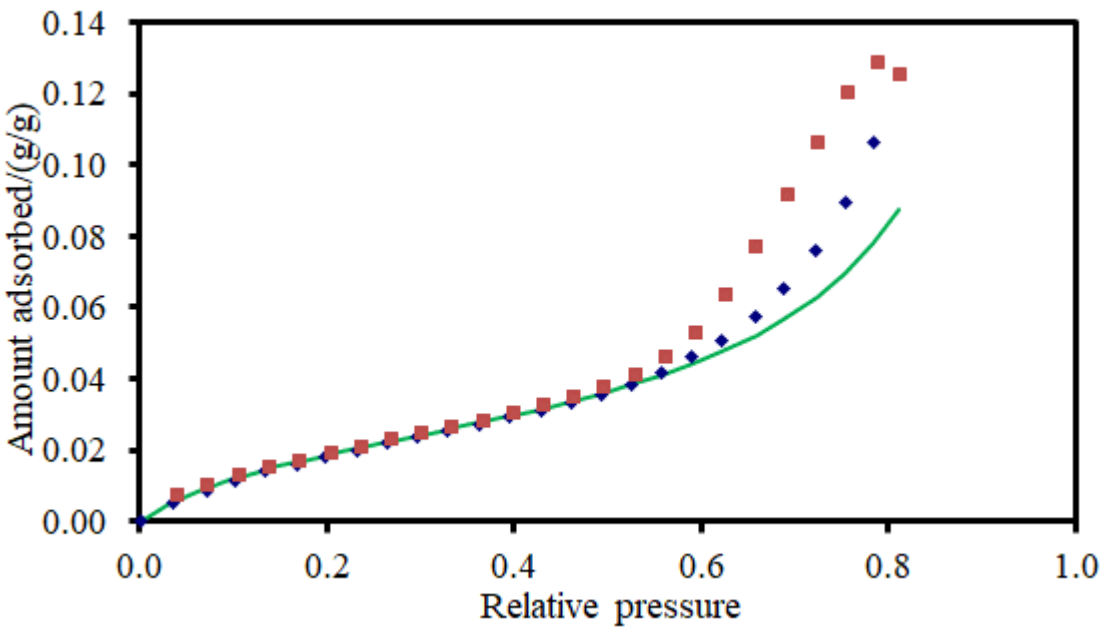

Table 2. Fractal dimensions obtained from the fractal BET and fractal FHH fits to experimental isotherms for fresh samples of G1.

Adsorbate	**Fractal BET surface fractal dimension**	**Length-scale range/nm**	**Fractal FHH surface fractal dimension**	**Length-scale range/nm**
Argon	2.23	<0.98	2.42	0.36-1.6
n-Butane (C4)	2.27	<0.55	2.30	0.55-1.2
Cyclohexane (cC6)	2.00	<1.2	2.60	0.20-5.7
n-Hexane (nC6)	2.00	<1.3	1.96	0.85-1.5
Nitrogen	2.32	<0.95	(i) 2.20 (ii) 2.55	<0.2 0.39-2.3
Propane (C3)	2.15	<1.0	2.26	0.64-1.1
Water	2.19	<0.52	2.28	0.31-0.62

The FHH model was generally fitted for the region of the isotherm data above the monolayer, except for nitrogen. It is noted that the fractal dimensions from the fractal FHH model in **Table 2** are similar to that for length-scales <1 nm from SAXS (in **Table 1**) for propane, n-butane, and water, plus nitrogen at low pressures. However, the surface fractal dimension from the FHH model fit to the argon and cyclohexane isotherms, and to higher pressures for the nitrogen isotherms, better matches the SAXS data for length-scales >1 nm.

The effective cross-sectional area for each adsorbate was calculated from the molar volume for a liquid at the conditions of the isotherm according to the method described by Gregg and Sing [12]. **Figure 8** shows a plot of the logarithm of the monolayer capacities for each adsorbate on G1 against the logarithm of the molecular cross-sectional area. While it can be seen that the other adsorbates broadly follow a linear trend, water is a clear outlier where the monolayer capacity is significantly lower based upon its molar volume and the trend for the other adsorbates. The surface fractal dimension for G1 obtained from the best-fit straight line to the data-points for the adsorbates other than water was 3.15±0.57, where the unrealistically

large value, and large error bar on that value (that does include the physically meaningful range of $2 \leq D \leq 3$), result from the scatter even for the adsorbates following the main trend. It is noted that argon and cyclohexane have apparent monolayer capacities lower than the trend line.

Figure 8. plot of the logarithm of the monolayer capacities for water (■) and the other (labelled) adsorbates (●) on G1 against the logarithm of the molecular cross-sectional area (σ). The dashed line shows a straight-line fit (with equation and coefficient of determination shown) to the data for the adsorbates other than water.

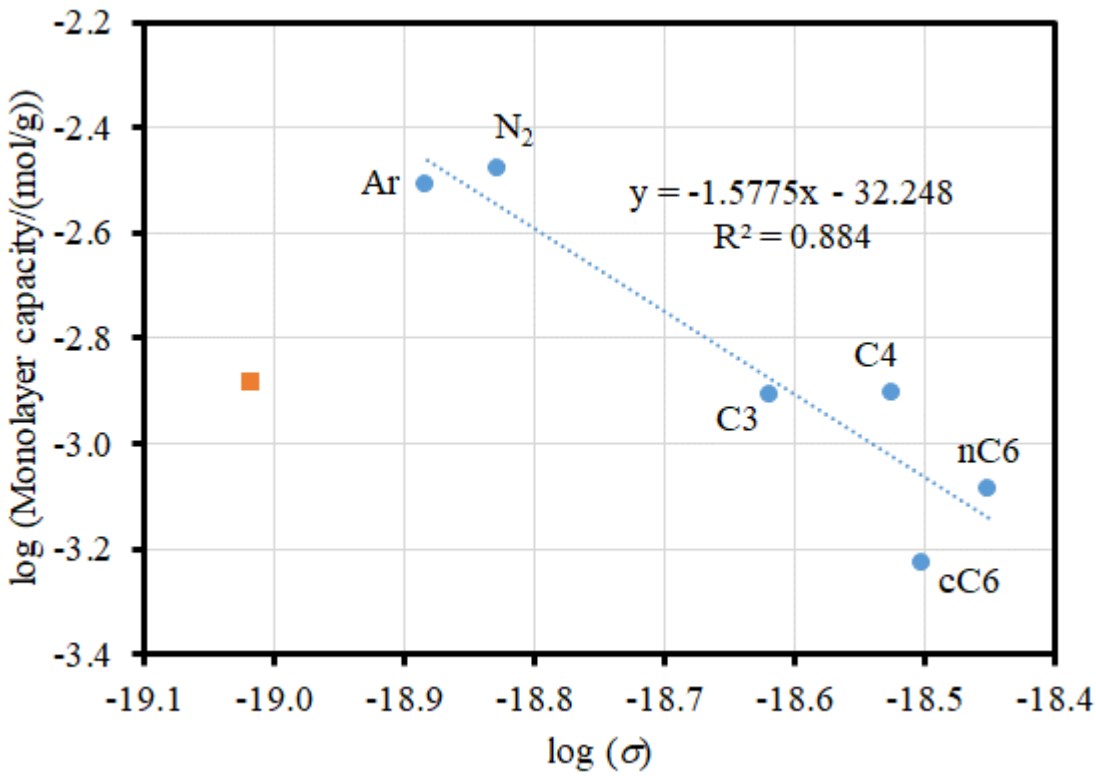

The nitrogen adsorption isotherms following water pre-adsorption were fitted to the fractal BET and fractal FHH isotherm equations, and the results are shown in **Table 3**. From **Table 3**, it can be seen that the fractal dimensions from both equations rise with increasing water saturation until a relative pressure of 0.794, and thereafter decline again, albeit less steeply.

Table 3. Fractal dimensions (±0.01) obtained from fits of the fractal BET and fractal FHH (high relative pressure) models to nitrogen adsorption isotherms after water pre-adsorption to the different relative pressures shown.

Water relative pressure	**BET fractal dimension after water adsorption**	**FHH fractal dimension after water adsorption**
0.497	2.31	2.55
0.646	2.36	2.57
0.794	2.47	2.63
0.871	2.42	2.60
0.914	2.41	2.62

The ratio of the volumes of the total adsorbed nitrogen before and after addition of water to different relative pressures was obtained from the horizontal plateau values at the top of the nitrogen isotherms in **Figure 6**. This volume fraction was the maximum nitrogen saturation for each sample in the presence of water adsorbed to different pressures. As the total specific volume was the same, within a small intra-batch variation (~1%), for each sample of G1 the nitrogen saturation was proportional to the volume of void space occupied by nitrogen at the top of the isotherm. The corresponding water saturation was estimated by subtracting the nitrogen saturation from unity. This latter calculation assumes that water did not block access to void space it did not actually occupy itself. **Figure 9** shows plots of the logarithm of the saturation, for either water or nitrogen, against the logarithm of the ratio of nitrogen monolayer capacities for before and after water adsorption. It can be seen that the data for nitrogen fits well to a straight line for all values of water saturation, while that for water itself only fits well to a straight line for the data for water relative pressures 0.497-0.794. However, the overall form of the variation of the data for water itself is similar to that observed by Pfeifer et al. [29] on porous silica. The fractal dimension for the surface obtained, from the film **equation (2),** for water is 2.14±0.02, while that obtained for nitrogen is 2.53±0.04. It is noted that the surface fractal dimension from the film equation for water is similar to that obtained from the fractal BET and fractal FHH models for water adsorption itself, and also from propane or butane adsorption, and from SAXS for length-scales <1 nm. The fractal dimension from the film equation for nitrogen is similar to that also obtained for nitrogen

using the fractal FHH isotherm fit for higher amounts adsorbed (at higher pressure above monolayer) and for SAXS for length-scales >1 nm.

Figure 9. Fractal film plots for the nitrogen side (a) and water side (b) obtained from volumes (V_0) of the ultimate total adsorbed nitrogen, and from the nitrogen monolayer capacities (V_m) from the fractal BET equation, before and after addition of water. The dashed lines are fits of straight lines to the ranges of data shown.

(a)

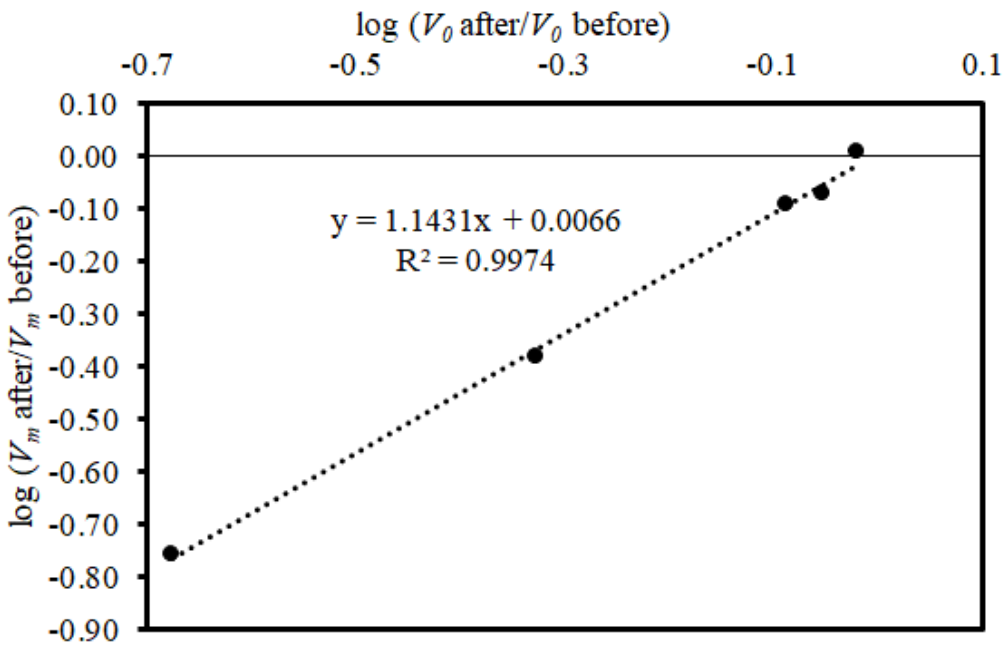

(b)

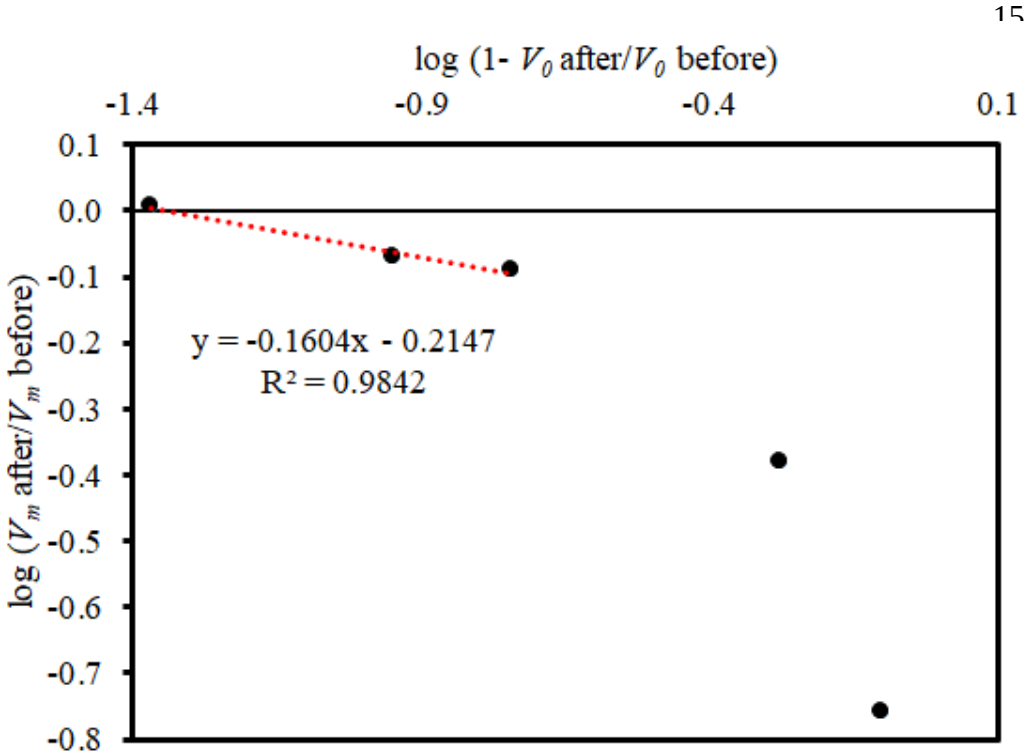

The relative pressures on the nitrogen isotherms where water adsorption causes deviations in the nitrogen data are revealed by the adjusted plots and are given in **Table 4**. It is noted that these deviations occur at pressures higher than the lower hysteresis closure point for nitrogen sorption. Also shown in **Table 4** are the relative pressures (P2) calculated from **equation (3)** for water adsorption into a pore with k=1, assuming that the relative pressure for water adsorption experiment (P1) corresponded to k=2, and, from **equation (4)**, the corresponding relative pressure for nitrogen adsorption in the same pore with the same meniscus geometry. From **Figure 6** and **Table 4**, it can be seen that water is condensing in pores that fill within the capillary condensation region for nitrogen but at relative pressures much lower than for nitrogen, though this discrepancy has decreased markedly at higher pressures. At higher pressures, the onset in the deviation between the nitrogen adsorption isotherms for before and after water adsorption at a relative pressure of 0.914 is that (~0.921) expected simply from the difference in adsorbate property factor between the two adsorbates.

Table 4. Relative pressures for intermediate water adsorption in serial experiments. Also shown are the corresponding relative pressure for water adsorption if it had occurred instead via a cylindrical meniscus for pores that would fill by advanced condensation at the actual relative pressure.

Water adsorption relative pressure (assuming *k*=2), P1	**Corresponding water adsorption relative pressure for *k*=1, P2**	**Nitrogen adsorption relative pressure (P3) equivalent to P1**	**Nitrogen adsorption relative pressure (P4) equivalent to P2**	**Estimated relative pressure for deviation of nitrogen desorption isotherms**	**Estimated relative pressure for deviation of nitrogen adsorption isotherms**
0.497	0.705	0.537	0.733	0.745	0.847
0.646	0.804	0.678	0.824	0.813	0.865
0.794	0.891	0.815	0.903	0.825	0.898
0.914	0.956	0.923	0.961	0.842	0.921

Figure 10 shows the cumulative BJH PSDs from the adsorption, obtained using a value of k=1 in **equation (3)**, for sample of G1 before and after water adsorption to a relative pressure

of 0.914. From a comparison of the two PSDs, it can be seen that the pore sizes left unfilled by water are in the range 10-15 nm. The relative pressure of 0.914 for water adsorption was chosen here as it gives rise to the same pore volume fraction left over without water saturation as the mercury saturation obtained by entrapment following porosimetry.

Figure 10. Cumulative BJH PSDs, obtained using a value of *k*=1 in equation (3), for sample of G1 before and after water adsorption to a relative pressure of 0.914.

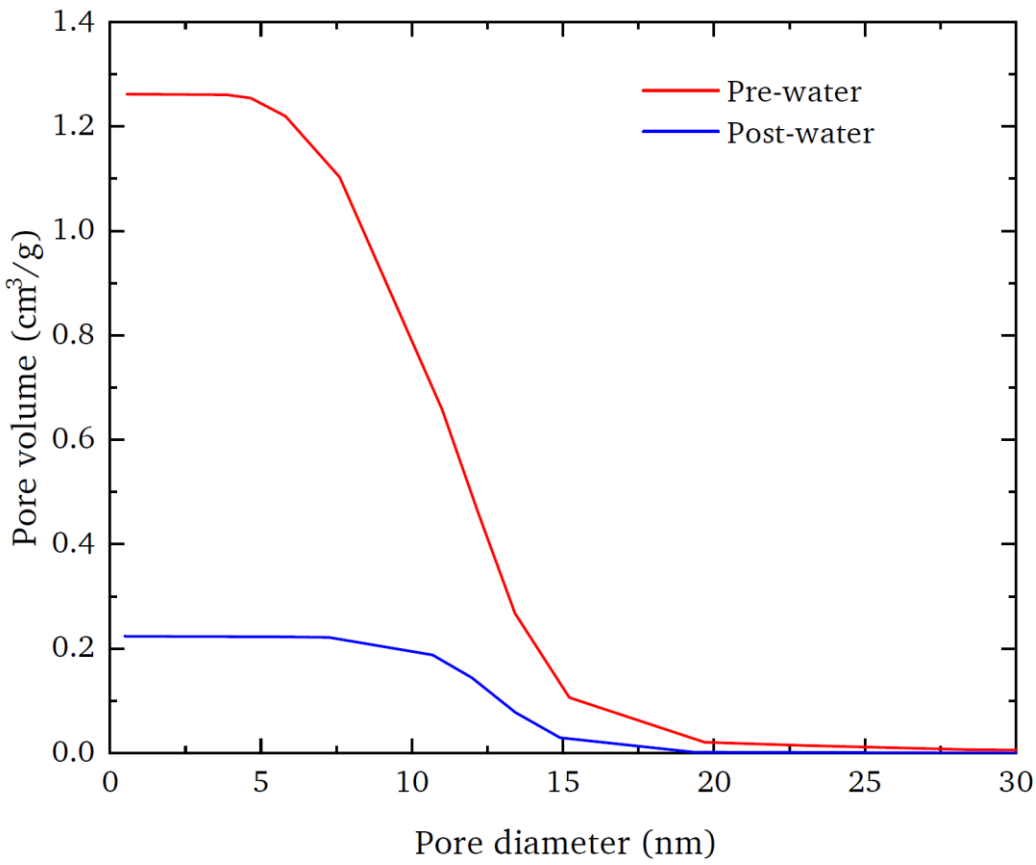

4.3 Serial water pre-adsorption, mercury porosimetry, and nitrogen adsorption

Figure 11(a) shows the raw mercury porosimetry data obtained for typical samples of G1 after the pellets had been initially dried at 350 °C and following pre-adsorption of water to a relative humidity of 0.85 by suspension above a saturated KCl solution. Since it is not possible to completely remove entrapped mercury following porosimetry, then the experiments after water pre-adsorption were, necessarily, run on different samples from the

same batch. In order to remove the small effects of intra-batch variability in pore volume between samples, the data obtained after water pre-adsorption was scaled such that a superposition of the lower part of the porosimetry curves was obtained. In the superposition process the sample mass for the curve after water adsorption was adjusted by a constant factor until the residuals with the data from before water adsorption were minimised. It can be seen from **Figure 11(a)** that an excellent superposition can be obtained for the curved regions in the initial intrusion, especially around the main percolation knee, and for the region where entrapment begins for extrusion when the extrusion curve deviates strongly into a more horizontal path from the previous more vertical drop.

However, it is noted that, in contrast, a good superposition cannot be obtained for the porosimetry curves obtained with and without water pre-adsorption when the amount of intruded mercury is plotted as fractional saturation (as seen in **Figure A2.2** in Appendix 2). This suggests that the shape of the top of the porosimetry curves is substantially altered by the water pre-adsorption. **Figure 11(a)** shows that the mercury entrapment for batch G1 declines only slightly following water pre-adsorption.

Figure 11. (a) Mercury intrusion and extrusion curves for G1 following drying at 350 °C (solid line) and following pre-adsorption of water to a relative pressure of 0.85 (×). **(b)** Variation with pore size, derived from Kloubek [32] correlation, of difference in incremental volume intruded between samples with and without water pre-adsorption.

(a)

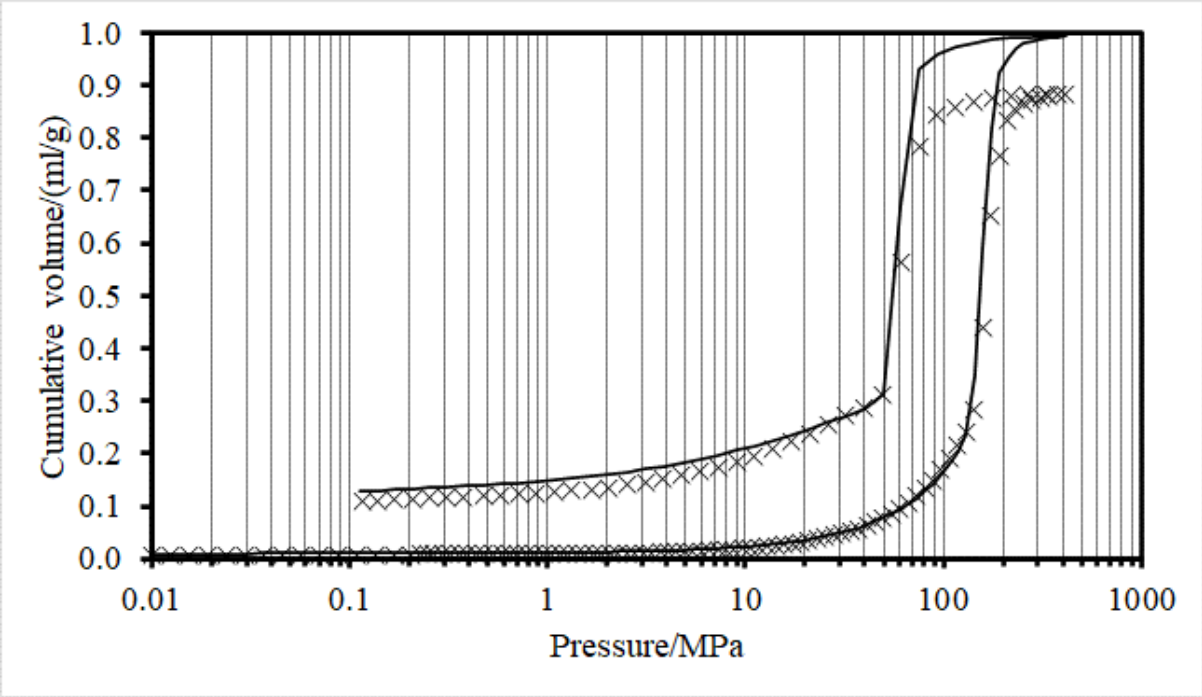

(b)

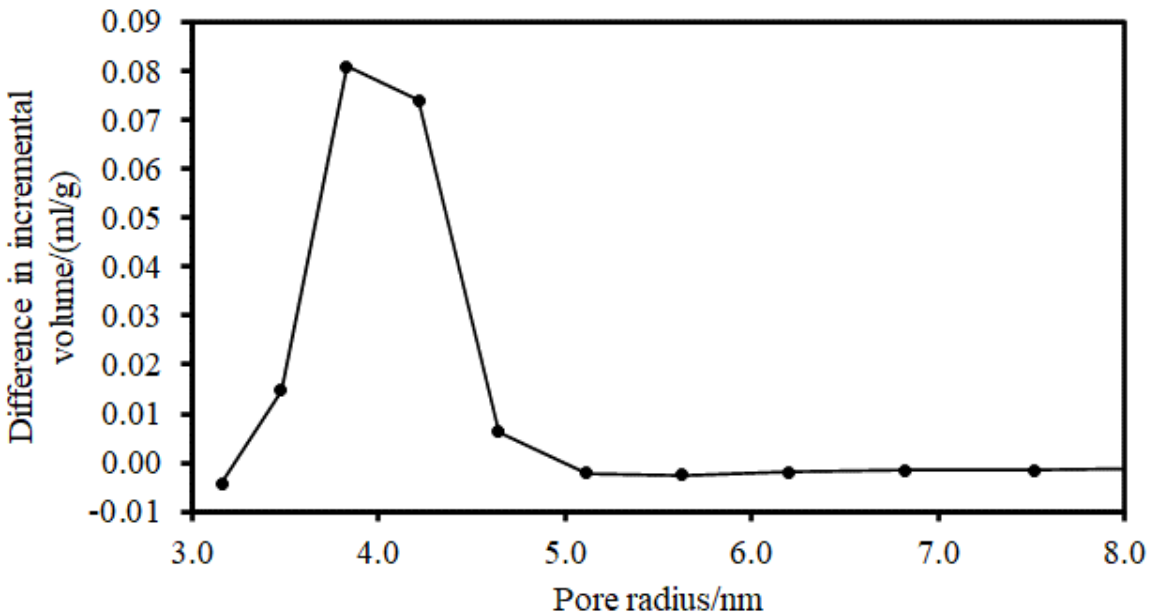

Figure 11(b) shows a plot of the variation with pore size of the differences in incremental intruded volume between before and after water pre-adsorption. The pore radius was obtained from the intrusion pressure using the Kloubek [32] correlations. Kloubek [32] developed calibrated versions of the Washburn equation [33] using mercury porosimetry data for model materials, namely a series of controlled pore glasses, for which the pore size of each had been independently determined from electron microscopy by Liabastre and Orr [34]. Given the Kloubek [32] correlations are empirically calibrated, it is noted that pore sizes derived from these correlations have experimental errors of ~4-5% associated with them. The results of analysing the raw mercury porosimetry data for G1, shown in **Figure 11(a)**, using the Kloubek [32] correlations are given in the **Appendix A2.3**. A good superposition was obtained for the main steps in the intrusion and extrusion curves for G1 using the Kloubek [32] correlations. These correlations were designed to remove contact angle hysteresis, and the level of superposition achieved shows that the two materials have similar contact angles to each other, and to the CPGs originally used to obtain the Kloubek [32] correlations. From **Figure 11(b),** it can be seen that water adsorption to a relative pressure of 0.85 leads to a loss in intrusion of pores of sizes peaking around ~4 nm for G1.

Figure 12(a) shows the cumulative BJH PSD, using a value of *k*=1 in **eq. (3),** obtained from the nitrogen adsorption isotherm for a typical sample of G1 after the pellets had been initially dried at 350 °C, and also following both pre-adsorption of water, to a relative humidity of 0.85, and mercury porosimetry. For consistency with the mercury porosimetry data, the nitrogen sorption data for the sample following water adsorption has been scaled by the same factor as for the corresponding mercury porosimetry data-set. It is noted that the difference in the cumulative nitrogen PSD pore volumes between before and after water adsorption is equal to the sum of the volumes lost to water (as shown by difference in ultimate intrusion volume in mercury intrusion curves) and entrapped mercury (taking account of the slightly less entrapment following water adsorption). This suggests that the mercury porosimetry and nitrogen sorption PSDs are a self-consistent set.

In order to further clarify the differences between the two PSDs shown in **Figure 12(a)**, **Figure 12(b)** shows a plot of the variation with pore radius of the difference in the differential of the PSDs shown in **Figure 12(a).** In order to obtain the differentials, the cumulative PSDs were fitted to sixth-order polynomials up to the largest pore size data-points just before the cumulative plot became horizontal, and the equations for these fits were differentiated to obtain the differential PSD. It can be seen that the differential difference plot is bimodal with a peak at a radius of ~4 nm and at ~6.5 nm. It is noted that the first (lower size) peak position for the nitrogen data for G1 given in **Figure 12(b)** and that for mercury in **Figure 11(b)** are similar. The second, larger pore size, peak in **Figure 12(b)** corresponds to the sizes of pores where mercury entrapment is occurring in Figure A2.3 in Appendix 2, and thus represent pores that nitrogen cannot enter due to presence of entrapped mercury. The valley between the peaks in **Figure 12(b)** corresponds to the region of overlap of the mercury intrusion and extrusion curves in Figure A2.3.

Figure 12. (a) Cumulative BJH PSDs, using a value of *k*=1 in eq. (3), obtained from nitrogen adsorption isotherms for G1 after the pellets had been initially dried at 350 °C (solid line), and also following pre-adsorption of water to a relative humidity of 0.85 and mercury porosimetry (●). **(b)** Differential difference plot obtained from the two PSDs shown in (a).

(a)

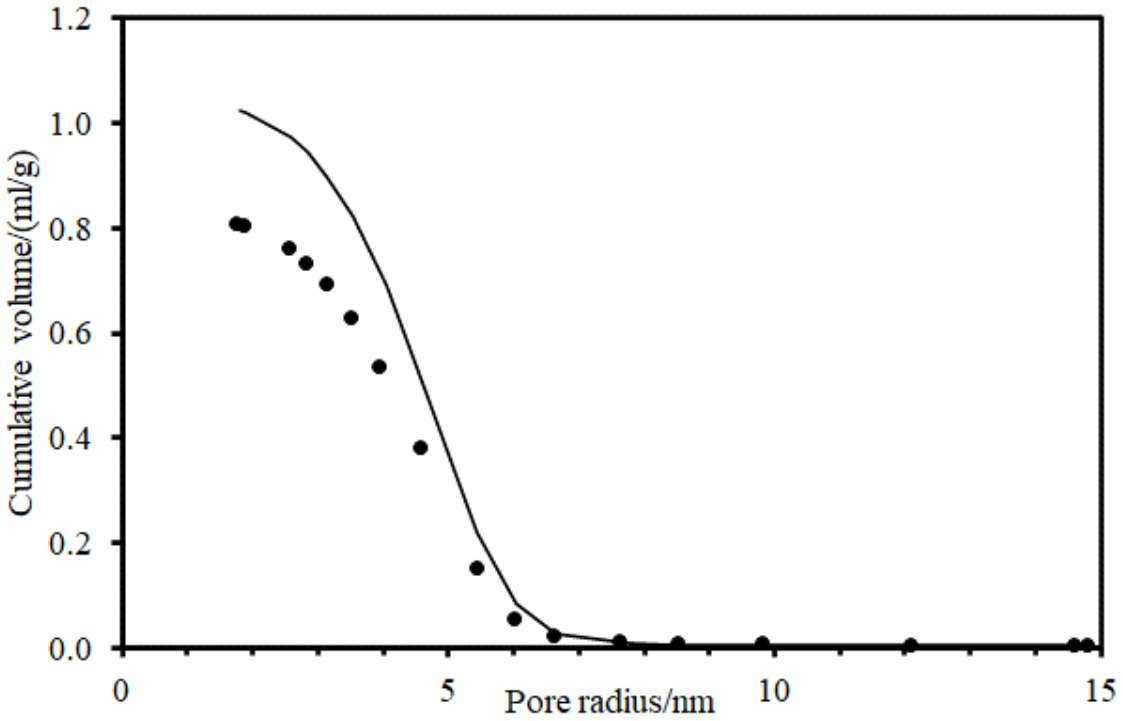

(b)

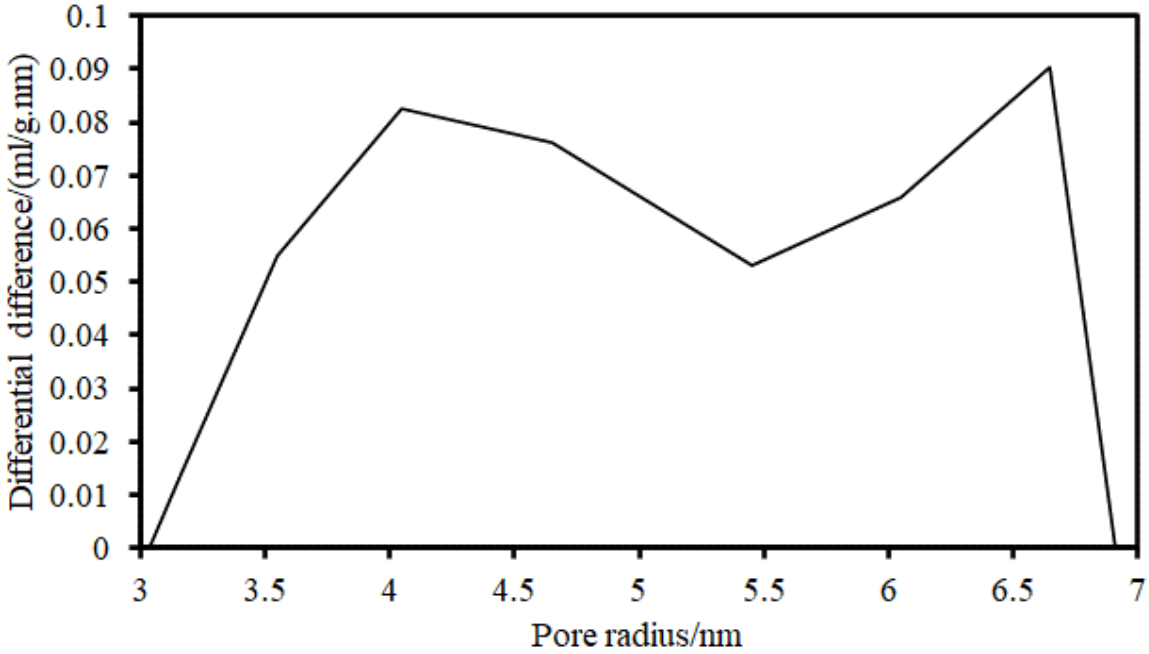

4.4 Dual liquid mercury-water DSC thermoporometry

Figure 13 shows the raw melting curve for sample of G1 containing both mercury and water following mercury entrapment during porosimetry and immersion in water afterwards. Small amounts of bulk liquids were added to sample to provide for internal references. It can be seen that both mercury and water within the sample pores show melting point depression relative to their respective bulk melting temperatures.

Figure 13. DSC melting curve for both mercury and water within the same sample of G1 following entrapment during porosimetry and immersion in water.

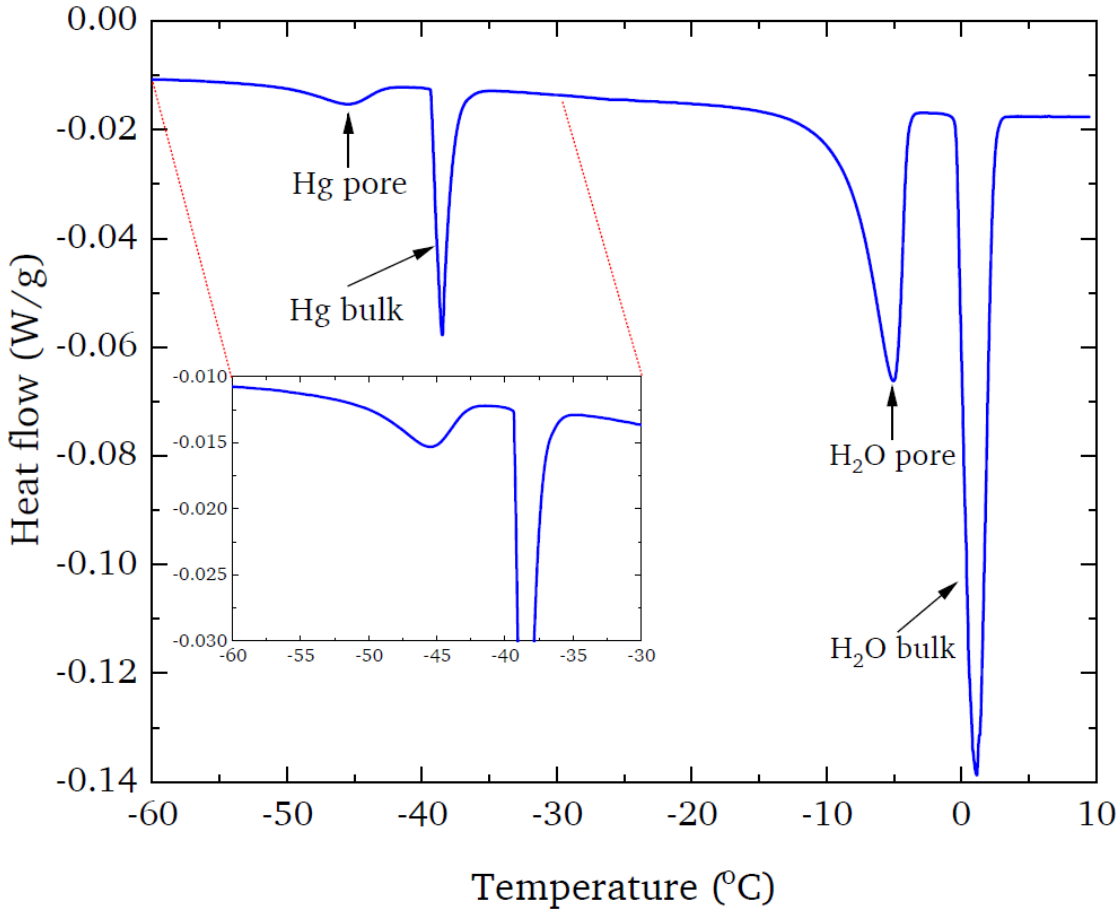

The melting temperatures in **Figure 13** have been converted to pore sizes assuming values of in *K* **equation (7)** of 90 K nm and 52 K nm, for mercury and water respectively. **Figure 14** shows a comparison of the BJH PSD obtained from the nitrogen adsorption isotherm measured after water adsorption to P/P_0=0.914, shown in **Figure 10**, and the PSD from DSC thermoporometry

for mercury entrapped in G1 shown in **Figure 13**. The modal volumes of each PSD have been renormalised to 1.0. From **Figure 14**, it can be seen that there is good overall agreement between the PSDs from nitrogen and mercury methods for the pore space left vacant after water adsorption to P/P_0=0.914.

Figure 14. Comparison of the BJH PSD obtained from the nitrogen adsorption isotherm measured after water adsorption to P/P_0=0.914, shown in **Figure 10**, and the PSD from DSC thermoporometry for mercury entrapped in G1 shown in **Figure 13**.

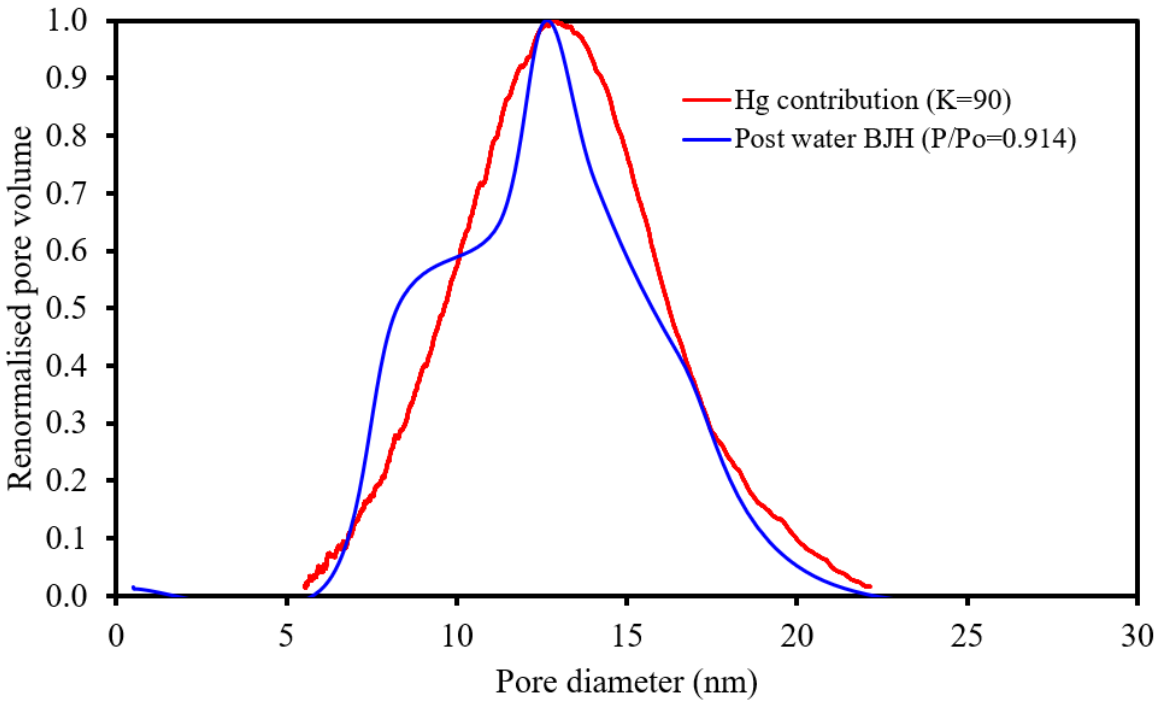

Figure 15(a) shows the PSD for the region occupied by water adsorbed to a relative pressure of 0.914 obtained by subtracting the nitrogen adsorption BJH PSD (using *k*=1 in **eq. (3)**) obtained after water adsorption from the corresponding PSD from nitrogen adsorption beforehand. The data for two separate suites of experiments on two different samples from batch G1 are shown to give an idea of inter-sample variability. In **Figure 15(a)**, this difference PSD is also compared with the PSD for the adsorbed water itself using DSC thermoporometry with a *K* value of 52 K nm in **equation (7)**. From a comparison of **Figure 14** and **Figure 15(a)**, this would suggest that the mercury occupies the largest pores in the sample, of sizes generally greater than ~10 nm, while the water occupies the smallest pores, generally less than ~10 nm. In contrast, **Figure 15(b)** shows the PSD for the region occupied by water adsorbed to a relative

pressure of 0.914 obtained by subtracting the nitrogen adsorption BJH PSD, obtained using *k*=2 in **eq. (3)**) for experimental data for after water adsorption, from the corresponding PSD from nitrogen adsorption before water addition. Also shown is the PSD for the adsorbed water itself using DSC thermoporometry with a *K* value of 95 K nm in **eq. (7)**. In this case, the water would appear to occupy the same sized pores as mercury in **Figure 14.**

Figure 15. PSD for the region occupied by water adsorbed to a relative pressure of 0.914 obtained by subtracting the nitrogen adsorption BJH PSD (using **(a)** *k*=1 or **(b)** *k*=2 in **eq. (3)**) obtained after water adsorption from the corresponding PSD from nitrogen adsorption beforehand. Data for experiments on two different samples (1 and 2) from batch G1 are shown to give an idea of inter-sample variability. Also shown is the PSD for the adsorbed water itself using DSC thermoporometry with a *K* value of **(a)** 52 or **(b)** 95 K nm in **eq. (7)**.

(a)

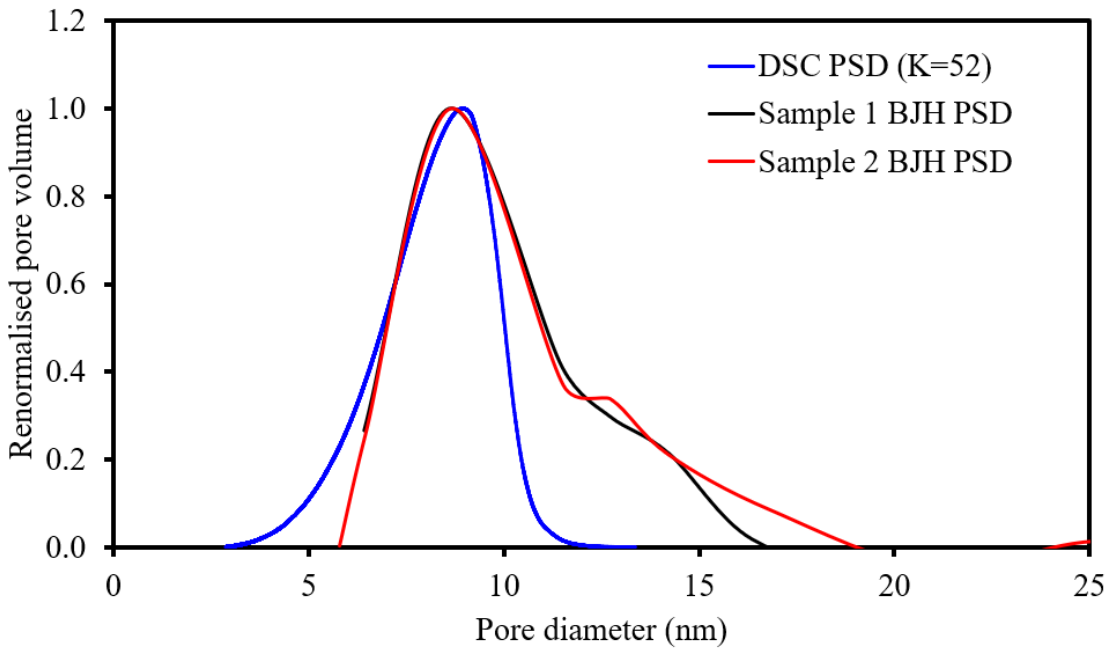

(b)

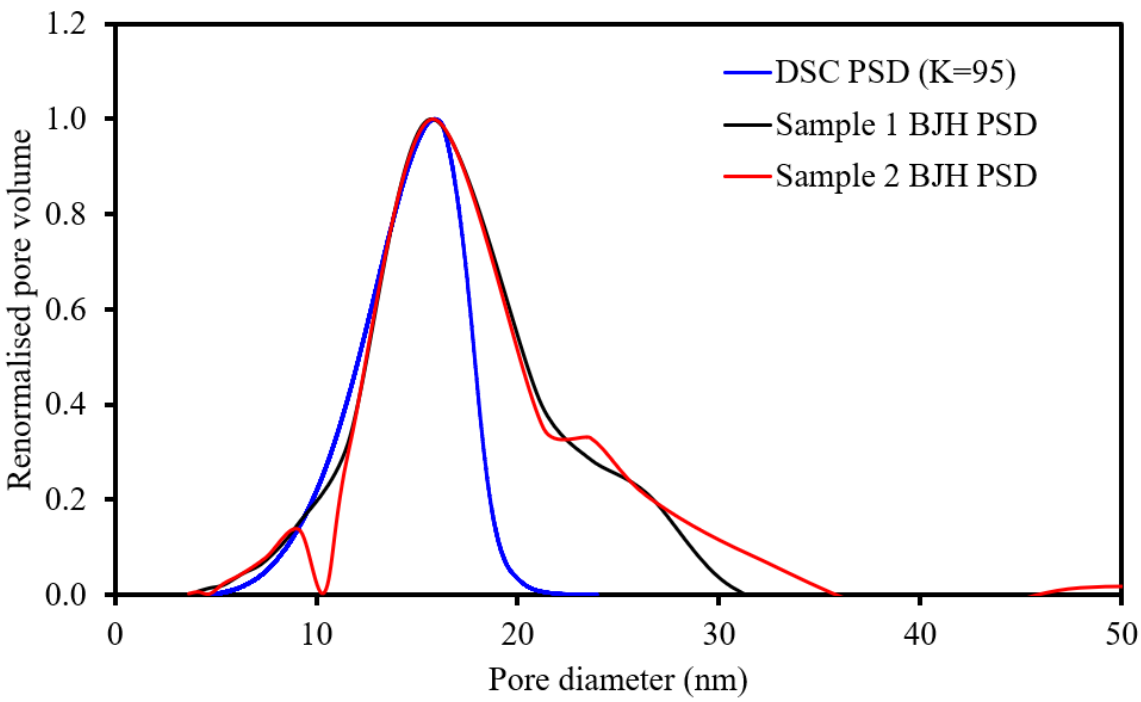

4.5 Integrated nitrogen sorption and mercury porosimetry

Figure 16 shows a comparison of the DSC thermoporometry PSD (using *K*= 90 K nm in **eq. (7)**) for the void space occupied by entrapped mercury following porosimetry, with the PSD for that same void space estimated from the difference in the BJH PSDs (using *k*=1 in eq. (3)) obtained from nitrogen adsorption isotherms measured before and after mercury porosimetry. The volume of the modal pore size in each distribution has been renormalised to 1.0. It can be seen that there is good agreement between the modal pore sizes obtained by the two methods but the width of the mercury thermoporometry PSD is wider than the nitrogen difference PSD.

Figure 16. Comparison of the DSC thermoporometry PSD for the void space in G1 occupied by entrapped mercury following porosimetry, with the PSD for that same void space estimated from the difference in the BJH PSDs (using *k*=1 in **eq. (3)**) obtained from nitrogen adsorption isotherms measured before and after mercury porosimetry

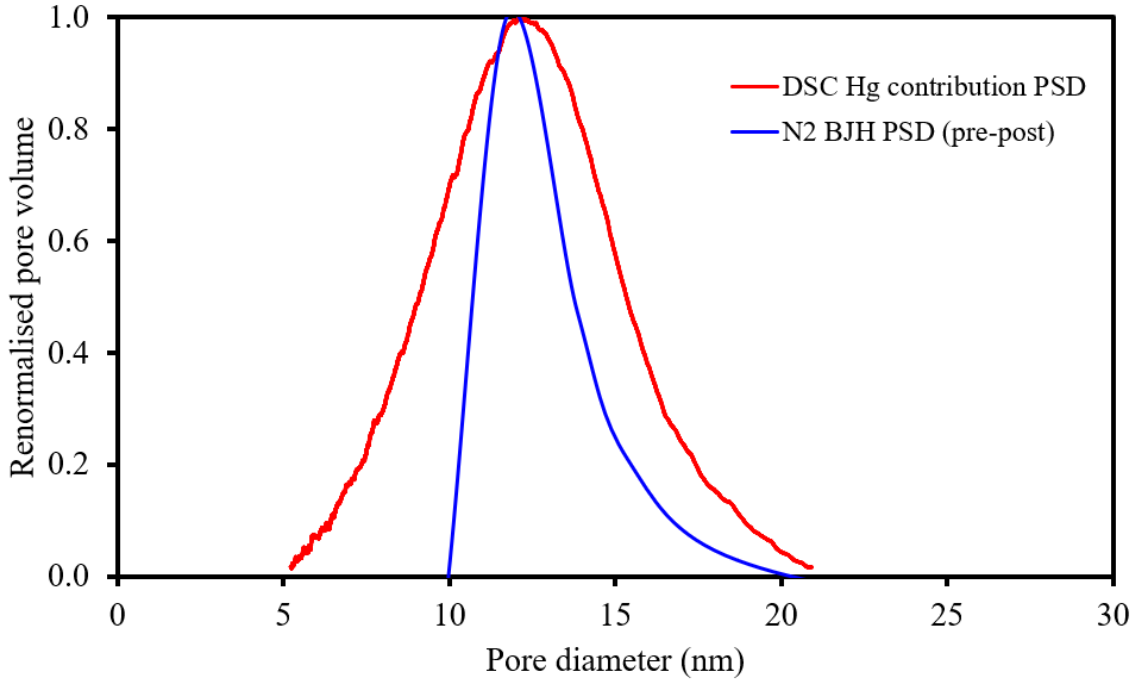

5 DISCUSSION

The comparison of the adsorption behaviour of water with a range of different adsorbates has revealed its particular idiosyncratic behaviour for the test case silica material. In the multi-layer region, the amount of adsorption of water, for the surface as a whole, is much lower than that which might be expected, for an adsorbate with its particular size, from the general trend for other, but less polar, adsorbates. However, the similarity between the surface fractal dimension from SAXS for shorter length-scales, and that from a fit of the fractal BET equation to the water isotherm, suggests that the growth of the multi-layer of water that does occur is in line with that expected from the BET model. This contrasts with the adsorption behaviour of n-hexane and cyclohexane which gives rise to apparent surface fractal dimensions lower than that for water, as might be expected if adsorption was seeded only at a few sparsely distributed high energy sites and proceeded just by addition of adsorbate only to sites immediately adjacent to itself, to, maybe, form a radially-expanding ‘dome-shape’. In that case the number of sites for adsorption would increase for each successive layer, leading to a relative under-estimate of fractal dimension, as seen for hexane molecules.

The structural analysis of the pre-adsorbed water phase by serial nitrogen adsorption is also consistent with adsorbed water forming a more dispersed film, rather than discrete ganglia. The variation of the water film volume with its surface area, according to the analysis of the nitrogen data using the model of Pfeifer et al. [29], was found to be consistent with that expected for film growth on a surface with a fractal dimension the same as that obtained from the water isotherm itself and SAXS (for length-scales <1 nm). If, instead, the water had been adsorbing in small, isolated ganglia, then, once frozen, these would have enhanced the surface roughness as perceived by the nitrogen, and the ‘film’ fractal dimension would have appeared anomalously high.

In contrast, in the higher reaches of the adsorption isotherms, where the presence of hysteresis indicates non-reversible capillary condensation has commenced for both nitrogen and water, it was found that water adsorption at lower pressure affects the nitrogen adsorption at higher corresponding parts of its hysteresis loop region. This suggests water fills the smallest pores at lower pressures than expected compared to nitrogen, even after the differences in adsorbate property factor are taken into account. A possible explanation is that, despite the more limited overall adsorption of water in the multi-layer region, that adsorption is relatively localised within the smaller pores, thereby making the multi-layer thicker and the core volumes correspondingly smaller than for nitrogen, thereby leading to the earlier onset of capillary

condensation there. At the uppermost reaches of the isotherms, the spatial disposition of water and nitrogen within the void space probably becomes more similar, since capillary condensation occurs at the expected corresponding relative pressures for pores of a certain size.

In contrast to water, the FHH plot for nitrogen suggests its adsorption only follows simple multi-layer build-up on the silica surface roughness for the very lowest pressure region of the isotherm. The similarity of the fractal dimension from FHH and SAXS over larger length-scales suggests that, thereafter, nitrogen adsorption follows the envelope surface of the packing of sol particles seen in the AFM images. This is a similar effect to that suggested by Tang et al. [35] for nitrogen adsorption on a close packing of smooth bovine serum albumin particles. As with this previous work, the change to an apparently larger fractal dimension, than for the silica particle surface roughness, may be due to the constraints on the occupancy numbers of successive upper layers of adsorbate that arise within the collars, or necks, formed at junctions between packing particles. A V-shaped profile collar region would have the same impact, of reducing the numbers of adsorption sites in successive layers, as the isolated pyramidal stacks of adsorbate envisaged in previous work on adsorption of nitrogen on flatter profile, but more chemically heterogeneous, silica surfaces [28].

It has been seen that the cumulative intrusion and extrusion curves from mercury porosimetry for samples of G1, that are initially dried, diverge at the top of the curves from the corresponding data for the same samples which have water pre-adsorbed to a relative humidity of 0.85. The subsequent analysis of these curves suggests that pre-adsorption of water has filled-up, and thereby prevented mercury intrusion within, pores of sizes only up to ~4 nm for G1. It is noted that the core pore sizes obtained from the Kelvin equation (**eq. 3**) for capillary condensation of water, at 296 K and relative pressure of 0.85, with cylindrical sleeve (k=1) and hemispherical (k=2) meniscus geometries, are 3.2 nm and 6.4 nm, respectively. The BET coverage equation suggests that the statistical first layer coverage for G1 at a relative pressure of 0.85 is 95.3%, suggesting at least a monolayer had built up at condensation, giving rise to a t-layer correction of at least 0.6 nm. Hence, this suggests water is adsorbing with a cylindrical sleeve meniscus geometry for G1. Capillary condensation via a hemispherical meniscus can arise from the dead-ends in pores, or be initiated from filled neighbouring pores, or even from advanced condensation. In an inter-connected pore network, the filling of the smallest pore via a cylindrical sleeve meniscus will present a hemispherical meniscus to the adjoining pores, thereby potentially facilitating axial filling of such pores at lower pressure than otherwise. If the neighbouring larger pore diameter is less than twice the small pore, then it will also fill at the

same pressure step via advanced condensation. If there is a significant spatial correlation in pore sizes, then these pore-pore co-operative effects will lead to more pores filling than would happen if the same pores were more widely dispersed within the network amidst larger pores. The aforementioned results thus suggest that the pores of sizes less than 5 nm in G1 are well-dispersed and only adjoined by much larger pore bodies that do not fill via either meniscus geometry at relative humidity of 0.85. This suggests a network of the type where narrow necks are interspersed between wide pore bodies. Indeed, G1 is a sol-gel silica formed by the agglomeration of tiny silica sol spheres, where wide pore bodies are formed in the central gaps between sol particles and these gaps are separated by narrow necks. This structure is evident in AFM images of samples of G1 shown in **Figure 5**.

For sample G1, the loss of ~10-15 % of ultimate intruded volume in mercury porosimetry following water adsorption did not affect the level of mercury entrapment obtained very much at all. This is possible if that entrapment is arising from macroscopic structural heterogeneities whereby regions of large pores are surrounded by a 'sea' of small pores [36]. The loss of a sub-set of small pores in this sea will not affect entrapment in the larger pores. Light microscopy studies of pellets of G1 following entrapment have shown that the mercury ganglia have macroscopic dimensions [37]. The slight decline in entrapment for G1 following water adsorption may be because the adsorbed water creates some more dead-ends with free mercury menisci from which retraction can be more easily initiated without the need for snap-off.

It is noted that the PSD from dual-liquid DSC thermoporometry for entrapped mercury in **Figure 14** used a value of the mercury Gibbs-Thomson parameter of 90 K nm. This is the value obtained previously by Bafarawa et al. [38] for melting of mercury via a hemispherical meniscus in a CPG. Hence, the value of K cannot be any larger, and thus the pores filled with entrapped mercury cannot be any larger. According to **Figure 14**, the pores occupied by mercury are in the range ~10-20 nm. However, according to **Figure 15(b)**, this is also the pore size range occupied by the complementary liquid, water, in the same dual-liquid DSC thermoporometry experiment. The two liquids cannot simultaneously occupy the same pores, and so one of the PSDs in **Figure 14** and **Figure 15(b)** must be using incorrect key constants of proportionality in the master pore size equations. The fact that the sizes in the mercury DSC thermoporometry PSD cannot be made any larger suggests **Figure 15(b)** is the PSD in error. This means that the PSDs in **Figure 15(a)** must be the correct ones, because then water will be considered to occupy the complementary, smaller pores in G1, as might be expected as water is the wetting fluid. Further, the pore sizes occupied by water according to the PSD in **Figure**

15(a), is more in line with the sizes (<10 nm) of the smallest 70% of pores in G1 according to the mercury intrusion PSD in **Figure 11(b)**, obtained using the Kloubek [32] correlations, than are those according to **Figure 15(b)**.

The water DSC thermoporometry PSD in **Figure 15(a)** used a value of K=52 K nm. This PSD was consistent, in terms of modal pore size, with that obtained by subtracting the BJH PSD, assuming capillary condensation occurred via a cylindrical sleeve meniscus, for nitrogen adsorption isotherms obtained after water adsorption from that obtained beforehand. It is noted that, in **Figure 16**, the modal pore size obtained from the difference between the PSDs, also obtained assuming nitrogen capillary condensation via a cylindrical sleeve meniscus, during adsorption either side of mercury entrapment from porosimetry on the same sample, coincides with the modal pore size containing the entrapped mercury from DSC thermoporometry. Hence, overall **Figures 14-16** lead to a self-consistent set of PSDs assuming melting of mercury occurs via a hemispherical meniscus, while melting of water occurs via a cylindrical sleeve meniscus, and capillary condensation of nitrogen occurs via a cylindrical sleeve meniscus irrespective of whether complementary sets of pores are filled with frozen water or mercury, at the saturation levels of water and mercury tested (see **Figure 6**). Hence, both water and nitrogen condense via a cylindrical sleeve meniscus in G1. It is also noted that the value of K=52 K nm used here is consistent with the value of 52.4 K nm, as calculated by Schreiber et al. [3], using the definition of K in Equation (6) and the values for water at its normal melting temperature such that the molar volume υ is 18 cm^3mol^{-1}, the surface free energy γ_{sl} is 32 mJ m^{-2}, the bulk melting point T^0 is 273.15 K, and the latent heat of melting ΔH is 6.0 kJ mol^{-1}. In contrast, from a similar calculation, Rottreau et al. [4] obtained a slightly different value of K=49.5 K nm, but they used a value of surface free energy γ_{sl} of 30 mJ m^{-2}. However, the difference of ~5% in the estimates of K by this method, and uncertainty in the non-freezing layer thickness, are much smaller than the impact of the choice of meniscus geometry.

6 CONCLUSION

The multi-layer build-up of nitrogen and water both show idiosyncrasies compared to a basket of other adsorbates. Analysis of the surface area of the interface between, and complementary volumes of, a solid surface-adsorbed film and the residual pore space has shown that both water and nitrogen initially form multi-layer films on the silica. However, while that multi-layer build-up for water is concentrated in the smaller pores, in contrast, for nitrogen, it is more pervasive and rapidly becomes directed by the envelope surface of the packed bed of silica sol particles, rather than the surface roughness of individual constituent particles. Dual-probe thermoporometry or adsorption can be used to determine the correct mode of the phase transition used to characterise the pore structure of disordered mesoporous materials, without recourse to either model templated materials for calibration, or imaging methods.

ACKNOWLEDGEMENTS

This work was supported by the Engineering and Physical Sciences Research Council [grant number EP/R512059/1].

7 REFERENCES

[1] Rigby, S.P., *Structural Characterisation of Natural and Industrial Porous Materials: A Manual*, Springer International Publishing, Cham, 2020.

[2] V.M. Gun'ko, V.V. Turov, A.V. Turov, V.I. Zarko, V.I. Gerda, V.V. Yanishpolskii, I.S. Berezovska, V.A. Tertykh, Behaviour of pure water and water mixture with benzene or chloroform adsorbed onto ordered mesoporous silicas. Cent Eur J Chem 5(2) (2007) 420–454.

[3] A. Schreiber, I. Ketelsen, G.H. Findenegg, Melting and freezing of water in ordered mesoporous silica materials. Phys Chem Chem Phys 3 (2001) 1185-1195.

[4] T.J. Rottreau, C.M.A. Parlett, A.F. Lee, R.Evans, NMR cryoporometric measurements of porous silica: A method for the determination of melting point depression parameters of probe liquids. Micropor. Mesopor. Mat. 264 (2018) 265-271.

[5] O. Petrov, I. Furó, Curvature-dependent metastability of the solid phase and the freezing-melting hysteresis in pores. Phys Rev E 73 (2006) 011608.

[6] E.L. Perkins, J.P. Lowe, K.J. Edler, N. Tanko, S.P. Rigby, Determination of the percolation properties and pore connectivity for mesoporous solids using NMR cryodiffusometry. Chem Eng Sci 63 (2008) 1929-1940.

[7] I. Hitchcock, E.M. Holt, J.P.Lowe, S.P. Rigby, Studies of freezing-melting hysteresis in cryoporometry scanning loop experiments using NMR diffusometry and relaxometry, Chem. Eng. Sci. 66 (2011) 582-592.

[8] D.H. Everett, in: S.J. Gregg, K.S.W. Sing, H.F. Stoeckli (Eds.), Characterization of Porous Solids, Soc. Chem. Ind, 1979, p.229.

[9] G. Mason, The effect of pore lattice structure on the pore size distributions calculated from sorption isotherms using percolation theory, J. Colloid Interface Sci. 95 (1983) 277-278.

[10] N.A. Seaton, Determination of the connectivity of porous solids from nitrogen sorption measurements. Chem Eng Sci 46 (1991) 1895-1909.

[11] M. Parlar, Y.C. Yortsos, Percolation theory of vapour adsorption desorption processes in porous materials, J. Colloid Interface Sci. 124 (1988) 162-176.

[12] S.J. Gregg, K.S.W. Sing, Adsorption, Surface Area and Porosity. Academic Press Inc, London, 1982.

[13] S.P. Rigby, Recent Developments in the Structural Characterisation of Disordered, Mesoporous Solids. JMTR 62 (2018) 296-312.

[14] J.H. De Boer, The shapes of capillaries, In: D.H. Everett and F.S. Stone (Eds.), The structure and properties of porous solids, Butterworths Scientific Publications: London, U.K., 1958; p. 68.

[15] F. Rouquerol, J. Rouquerol, K. Sing, K., Adsorption by Powders and Porous Solids: Principles, Methodology and Applications. Academic Press, London, 1999.

[16] I. Hitchcock, S. Malik, E.M. Holt, S.P. Rigby, Impact of Chemical Heterogeneity on the Accuracy of Pore Size Distributions in Disordered Solids. J Phys Chem C 118 (2014) 20627-20638.

[17] L.H. Cohan, Sorption hysteresis and the vapor pressure of concave surfaces. J. Am. Chem. Soc. 60 (1938) 433-435.

[18] A.V. Neimark, P.I. Ravikovitch, Capillary Condensation in MMS and Pore Structure Characterization. Micropor Mesopor Mater. 44 (2001) 697−707.

[19] I. Hitchcock, J.A. Chudek, E.M. Holt, J.P. Lowe, S.P. Rigby, NMR Studies of Cooperative Effects in Adsorption. Langmuir 26 (2010) 18061-18070.

[20] M. Wu, K. Fridh, B. Johannesson, M. Geiker, Impact of sample crushing on porosity characterization of hardened cement pastes by low temperature calorimetry: Comparison of powder and cylinder samples, Thermochimica Acta 665 (2018) 11-19.

[21] S.P. Rigby, R.S. Fletcher, S.N. Riley, Characterisation of porous solids using integrated nitrogen sorption and mercury porosimetry. Chem Eng Sci 59 (2004) 41-51.

[22] R. Valiullin, I. Furó, Low-temperature phase separation of a binary liquid mixture in porous materials studied by cryoporometry and pulsed-field gradient NMR, Phys. Rev. E 66 (2002) 031508.

[23] R. Valiullin, I. Furó, Phase separation of a binary liquid mixture in porous media studied by nuclear magnetic resonance cryoporometry, J. Chem. Phys. 116 (2002) 1072-1076.

[24] J. Mitchell, S.C. Stark, J.H. Strange, Probing surface interactions by combining NMR cryoporometry and NMR relaxometry. J. Phys. D: Appl. Phys. 38 (2005) 1950-1958.

[25] K. Ishikiriyama, M. Todoki, K. Motomura, Pore size distribution (PSD) measurements of silica gels by means of differential scanning calorimetry. I Optimization for determination of PSD. J. Colloid Interface Sci. 171 (1995) 92-102.

[26] K. Ishikiriyama, M. Todoki, Pore size distribution (PSD) measurements of silica gels by means of differential scanning calorimetry. II Thermoporosimetry. J. Colloid Interface Sci. 171 (1995) 103-111.

[27] M. Wu, B. Johannesson, M. Geiker, Application of water vapor sorption measurements for porosity characterization of hardened cement pastes, Construction and Building Materials 66 (2014) 621-633.

[28] M. Watt-Smith, K.J. Edler, S.P. Rigby SP, An Experimental Study of Gas Adsorption on Fractal Surfaces. Langmuir 21 (2005) 2281-2292

[29] P. Pfeifer, G.P. Johnston, R. Deshpande, D.M. Smith, A.J. Hurd, Structure analysis of porous solids from preadsorbed films. Langmuir 7 (1991) 2833-2843.

[30] E.P. Barrett, L.G. Joyner, and P.P. Halenda, The Determination of Pore Volume and Area Distributions in Porous Substances. I. Computations from Nitrogen Isotherms. J Am Chem Soc, 1951. 73(1): p. 373-380 DOI: 10.1021/ja01145a126.

[31] W.D. Harkins, D. Jura, Surfaces of Solids. XII. An Absolute Method for the Determination of the Area of a Finely Divided Crystalline Solid. J Am Chem Soc 66 (1944) 1362-1366.

[32] J. Kloubek, Hysteresis in porosimetry. Powder Technol. 29 (1981) 63-73.

[33] E.W. Washburn, The dynamics of capillary flow, Phys. Rev. 17 (1921) 273-283.

[34] A.A. Liabastre, C. Orr, Evaluation of pore structure by mercury penetration. J Colloid Interface Sci 64 (1978) 1-18.

[35] P. Tang, N.Y.K. Chew, H.K. Chan, J.A. Raper, Limitation of determination of surface fractal dimension using N_2 adsorption isotherms and modified Frankel-Halsey-Hill theory, Langmuir 19 (2003) 2632-2638.

[36] N.C. Wardlaw, M. McKellar, Mercury porosimetry and the interpretation of pore geometry in sedimentary rocks and artificial models. Powder Technol 29 (1981) 127-143.

[37] S.P. Rigby, R.S. Fletcher, S.N. Riley, Determination of the cause of mercury entrapment during porosimetry experiments on sol-gel silica catalyst supports, Appl. Catal. A 247 (2003) 27-39.

[38] B. Bafarawa, A. Nepryahin, L. Ji, E.M. Holt, J. Wang, S.P. Rigby, Combining mercury thermoporometry with integrated gas sorption and mercury porosimetry to improve accuracy of pore-size distributions for disordered solids, J Colloid Interface Sci 426 (2014) 72-79.

APPENDIX A1. Adsorption isotherms on G1 for different adsorbates

Figure A1.1. Adsorption isotherm for argon at 87 K. The solid line shown is a fit of the fractal BET equation for relative pressures <0.65.

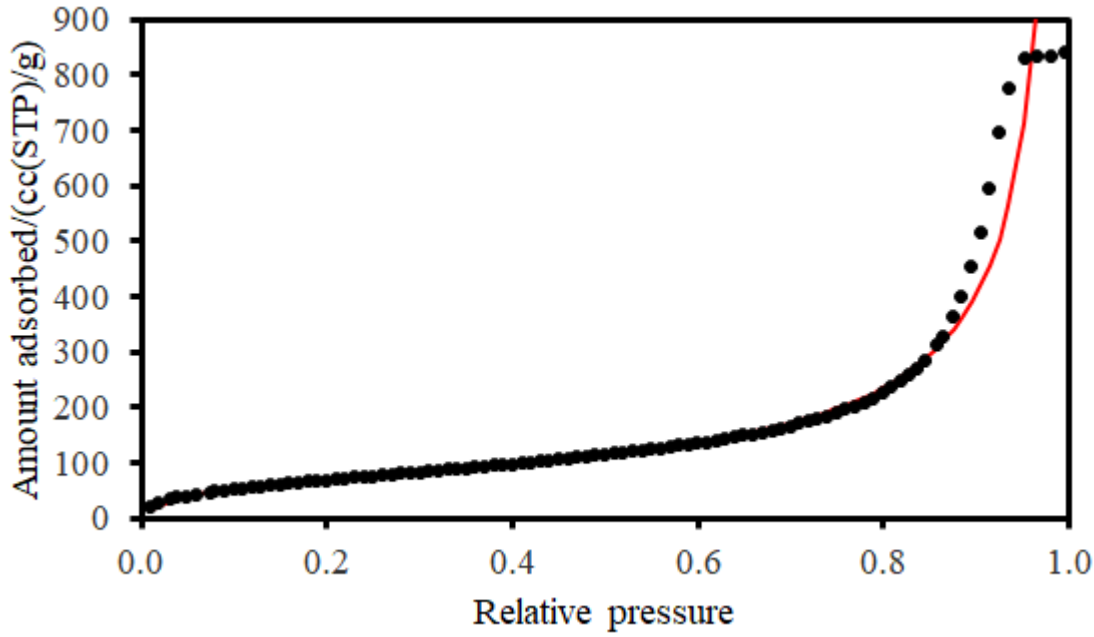

Figure A1.2. Adsorption isotherm for propane at 199 K. The solid line shown is a fit of the fractal BET equation for all isotherm.

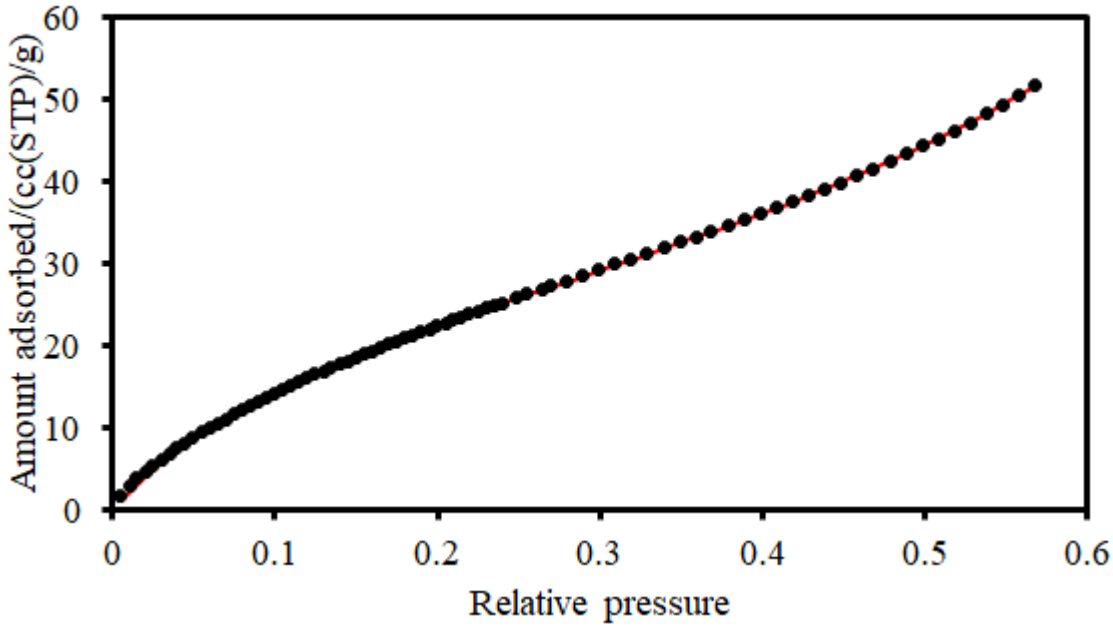

Figure A1.3. Adsorption isotherm for n-hexane at 273 K. The solid line shown is a fit of the fractal BET equation for relative pressures <0.6.

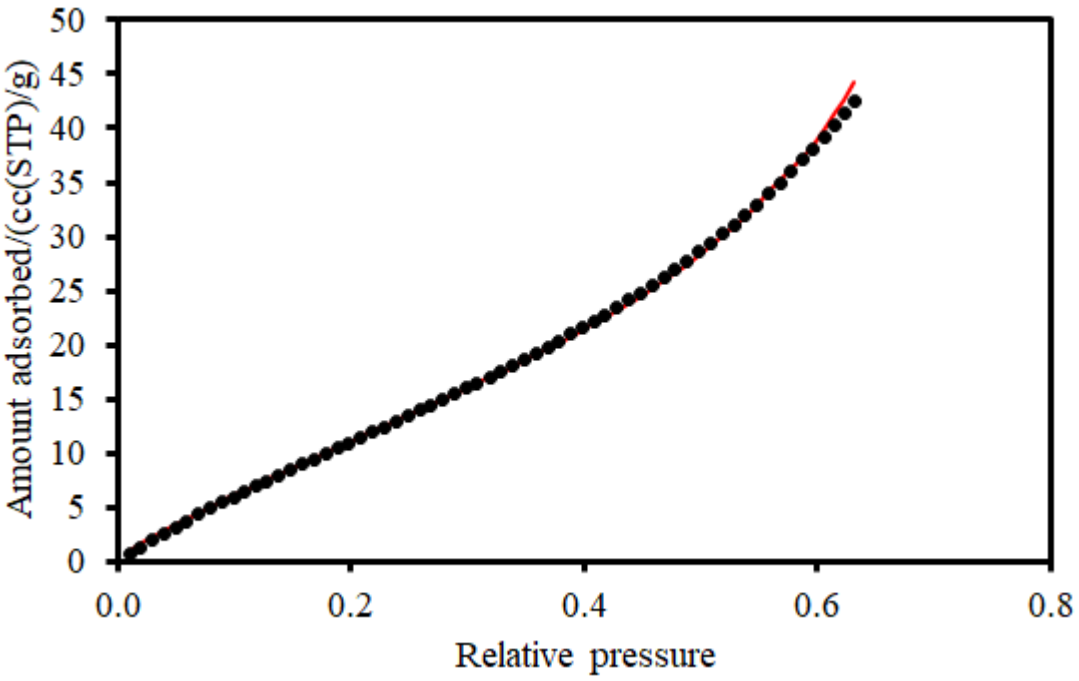

Figure A1.4. Adsorption isotherm for cyclohexane at 280 K. The solid line shown is a fit of the fractal BET equation for relative pressures <0.6.

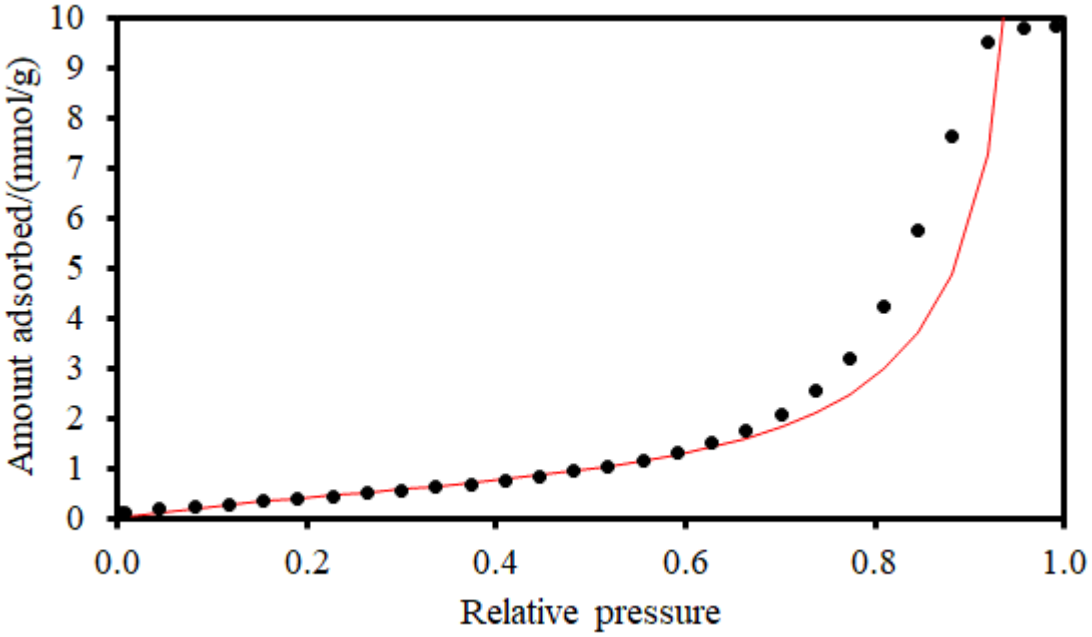

APPENDIX A2. Serial mercury porosimetry and water sorption

Figure A2.1. Close-up view of tops of mercury intrusion and extrusion curves for G1 following drying at 350 °C (solid line) and following pre-adsorption of water to a relative pressure of 0.85 (×).

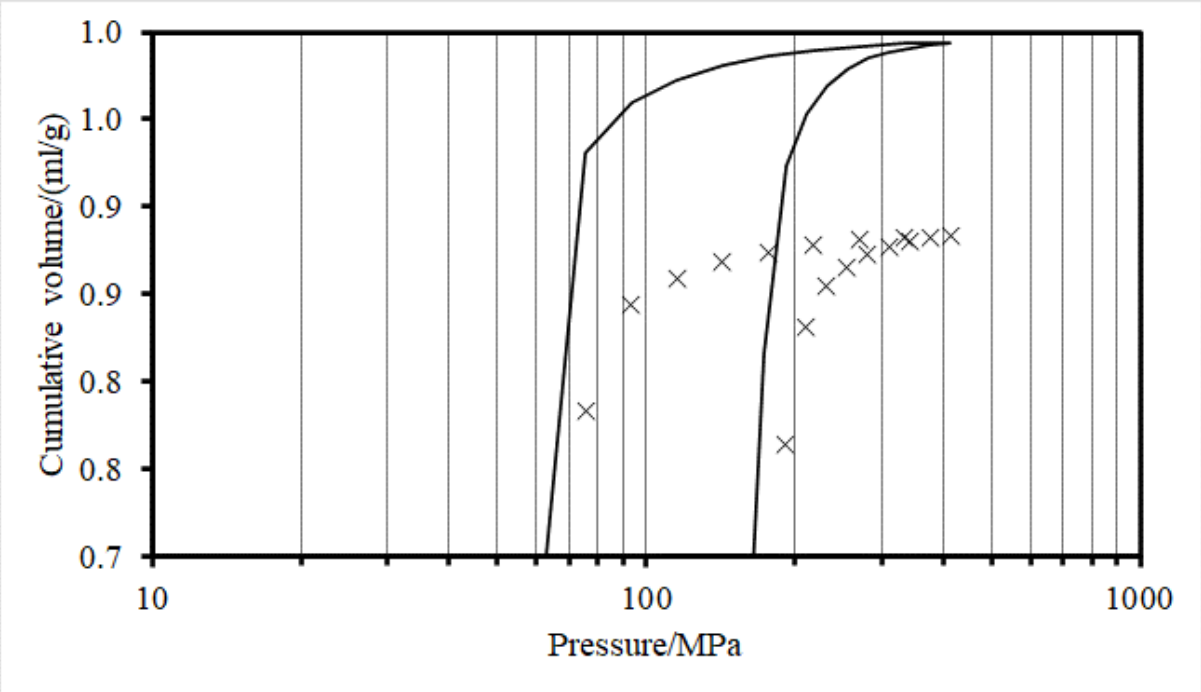

Figure A2.2. Fractional saturation (intruded volume at given pressure divided by ultimate intrusion volume) curves for mercury intrusion and extrusion for G1 following drying at 350 °C (solid line) and following pre-adsorption of water to a relative pressure of 0.85 (×).

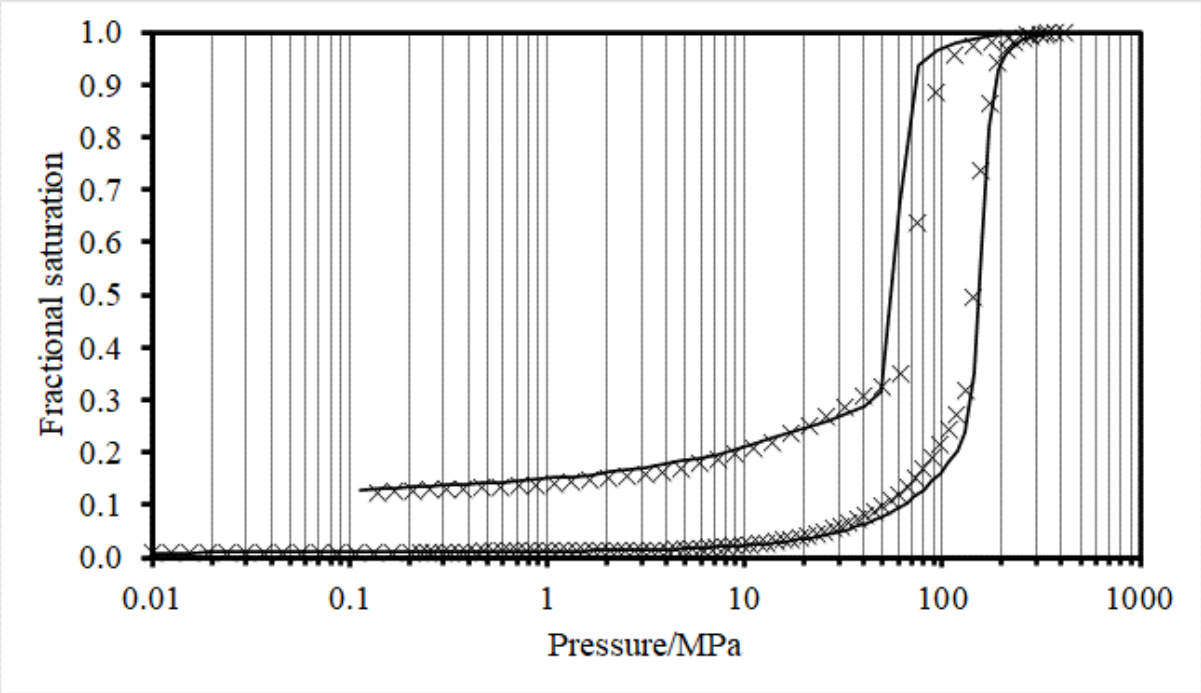

Figure A2.3 Mercury intrusion (lines) and extrusion (symbols) curves, analysed using the Kloubek [32] correlations, for G1 following drying at 350 °C (dashed line, ×) and following pre-adsorption of water to a relative pressure of 0.85 (solid line, +).